

Distance estimates for AGB stars from parallax measurements[★]

M. Andriantsaralaza¹, S. Ramstedt¹, W. H. T. Vlemmings², and E. De Beck²

¹ Theoretical Astrophysics, Division for Astronomy and Space Physics, Department of Physics and Astronomy, Uppsala University, Box 516, SE-751 20 Uppsala, Sweden

e-mail: miora.andriantsaralaza@physics.uu.se

² Department of Space, Earth and Environment, Chalmers University of Technology, Onsala Space Observatory, 439 92 Onsala, Sweden

Received 29 March 2022 / Accepted 24 August 2022

ABSTRACT

Context. Estimating the distances to asymptotic giant branch (AGB) stars using optical measurements of their parallaxes is not straightforward because of the large uncertainties introduced by their dusty envelopes, their large angular sizes, and their surface brightness variability.

Aims. This paper aims to assess the reliability of the distances derived with *Gaia* DR3 parallaxes for AGB stars, and provide a new distance catalogue for a sample of ~ 200 nearby AGB stars

Methods. We compared the parallaxes from *Gaia* DR3 with parallaxes measured with maser observations with very long baseline interferometry (VLBI) to determine a statistical correction factor for the DR3 parallaxes using a sub-sample of 33 maser-emitting oxygen-rich nearby AGB stars. We then calculated the distances of a total of ~ 200 AGB stars in the DEATHSTAR project using a Bayesian statistical approach on the corrected DR3 parallaxes and a prior based on the previously determined Galactic distribution of AGB stars. We performed radiative transfer modelling of the stellar and dust emission to determine the luminosity of the sources in the VLBI sub-sample based on the distances derived from maser parallaxes, and derived a new bolometric period-luminosity relation for Galactic oxygen-rich Mira variables.

Results. We find that the errors on the *Gaia* DR3 parallaxes given in the *Gaia* DR3 catalogue are underestimated by a factor of 5.44 for the brightest sources ($G < 8$ mag). Fainter sources ($8 \leq G < 12$) require a lower parallax error inflation factor of 2.74. We obtain a *Gaia* DR3 parallax zero-point offset of -0.077 mas for bright AGB stars. The offset becomes more negative for fainter AGB stars. After correcting the DR3 parallaxes, we find that the derived distances are associated with significant, asymmetrical errors for more than 40 % of the sources in our sample. We obtain a PL relation of the form $M_{\text{bol}} = (-3.31 \pm 0.24) [\log P - 2.5] + (-4.317 \pm 0.060)$ for the oxygen-rich Mira variables in the Milky Way. A new distance catalogue based on these results is provided for the sources in the DEATHSTAR sample.

Conclusions. The corrected *Gaia* DR3 parallaxes can be used to estimate distances for AGB stars using the AGB prior, but we confirm that one needs to be careful when the uncertainties on parallax measurements are larger than 20 %, which can result in model-dependent distances and source-dependent offsets. We find that a RUWE (re-normalised unit weight error) below 1.4 does not guarantee reliable distance estimates and we advise against the use of only the RUWE to measure the quality of *Gaia* DR3 astrometric data for individual AGB stars.

Key words. Stars: AGB and post AGB – Stars: distances – Parallaxes – Methods: statistical

1. Introduction

Distance is one of the most fundamental parameters in astronomy which lies at the basis of the analysis and interpretation of astronomical data. The *Gaia* mission (Gaia Collaboration et al. 2016b) aims to provide accurate measurements of the position, the parallax, and the proper motions of about 1 % of the stars in the Milky Way with accuracies 100 times better than its predecessor *Hipparcos*. Its astrometric instrument covers wavelengths between 330 and 1050 nm, defining the photometric G band (Carrasco et al. 2016; Gaia Collaboration et al. 2016b,a; van Leeuwen et al. 2017). The third *Gaia* data release (DR3), recently published by Gaia Collaboration et al. (2022), corresponds to an observing time of 34 months. The corresponding astrometry was published in an early third data release (Gaia Collaboration et al. 2021, hereafter eDR3), with nominal par-

allax uncertainties of 0.02 – 0.03 mas for $G < 15$, 0.07 mas at $G = 17$, 0.5 mas at $G = 20$, and 1.3 mas at $G = 21$ mag. We note that the values of all the parameters relevant to this work (e.g. parallax, parallax error, G magnitude) are identical in the *Gaia* eDR3 and DR3 catalogues for the sources discussed in this paper.

Determining the distances to asymptotic giant branch (AGB) stars using parallaxes measured with optical telescopes such as *Gaia* is, however, not a simple task. Comparative studies such as the analysis by Xu et al. (2019) based on *Gaia* data release 2 (DR2; Gaia Collaboration et al. 2018) show that the precision of the *Gaia* parallaxes depends on the colour of the star: the redder the star, the larger the errors. This is because red stars are usually larger, show more surface brightness variation, and have more dust. This is true for AGB stars. The AGB phase is the evolutionary stage at which low-to-intermediate-mass stars lose mass through slow and massive stellar winds, with mass-loss rates reaching up to $10^{-4} M_{\odot} \text{ yr}^{-1}$ (Höfner & Olofsson 2018). The material ejected from the star forms a large envelope mainly

[★] Table C.1 is only available in electronic form at the CDS via anonymous ftp to cdsarc.u-strasbg.fr (130.79.128.5) or via <http://cdsweb.u-strasbg.fr/cgi-bin/qcat?J/A+A/>

consisting of molecules and dust, called the circumstellar envelope (CSE). Therefore, interstellar and circumstellar dust both contribute to making AGB stars nearly invisible in the optical range of the electromagnetic spectrum. In addition, AGB stars are large objects, having angular sizes on the order of, or larger than, their respective parallaxes for the nearby ones (e.g. Chiavassa et al. 2020). Moreover, observations and simulations of AGB stars show that they possess large convective cells on their surfaces, which can shift the photocentre and thus introduce additional uncertainties to the measured parallaxes (Chiavassa et al. 2018). Furthermore, observations of bright sources can lead to instrumental saturation, resulting in less accurate astrometric measurements (El-Badry et al. 2021). This applies to AGB stars, as they are intrinsically bright objects.

An alternative method for parallax measurement consists of observing maser emission using very long baseline interferometry (VLBI). This method can yield a parallax precision of $\sim 10 \mu\text{as}$, comparable to or even better than *Gaia* (e.g. Reid & Honma 2014). However, it can only be used to determine the distance of known maser-emitting sources, which represent only a small number of AGB stars. Comparing the VLBI parallaxes with the *Gaia* DR3 parallaxes is therefore critical to get a better idea of the actual errors on the latter (van Langevelde et al. 2018; Xu et al. 2019) in order to infer better distance estimates for a large sample of AGB stars.

The main objective of this work is to determine the distances of ~ 200 nearby AGB stars that are part of the DEATHSTAR sample, described in Sect. 2. To attain this goal, this paper is divided into four main parts. First, the *Gaia* DR3 parallaxes were calibrated using a sub-sample of maser-emitting oxygen-rich AGB stars that have independent parallax measurements obtained using VLBI techniques (Sect. 3). We then calculated the distances of the sources in the DEATHSTAR sample using the newly corrected *Gaia* DR3 parallaxes following a Bayesian approach (Sect. 4). In Sect. 5 we present an alternative method to determine the distances of Mira variables in the DEATHSTAR sample: a new bolometric period-luminosity (PL) relation based on the aforementioned independent maser parallax measurements of the sub-sample of VLBI sources. Finally, we compiled a new distance catalogue for the ~ 200 nearby AGB stars in the DEATHSTAR sample in Sect. 6, based on the results in Sects. 4 and 5, and using alternative distance determination methods in the literature, when needed. Section 7 closes the paper with a summary and conclusions.

2. The sample

The DEATHSTAR¹ sample consists of ~ 200 nearby AGB stars. The first publications of the DEATHSTAR project present the CO observations of ~ 70 southern sources (Ramstedt et al. 2020; Andriantsaralaza et al. 2021). The source selection and completeness of the full DEATHSTAR sample is discussed in Ramstedt et al. (2020). The C-type stars ($C/O > 1$) are all brighter than 2 mag in the *K* band and were taken from Schöier & Olofsson (2001). The M-type stars ($C/O < 1$) were collected from either the General Catalogue of Variable Stars (GCVS; Samus' et al. 2017, non-Miras) or González Delgado et al. (2003, Miras). The selection criteria for the M-type stars taken from the GCVS are a quality flag 3 (high quality) in the *IRAS* 12, 25, and $60 \mu\text{m}$ bands, and a $60 \mu\text{m}$ flux ≥ 3 Jy. The S-type stars ($C/O \approx 1$) were also selected based on the quality of their *IRAS* flux measurements at 12, 25, and $60 \mu\text{m}$, and on the presence of Tc in their

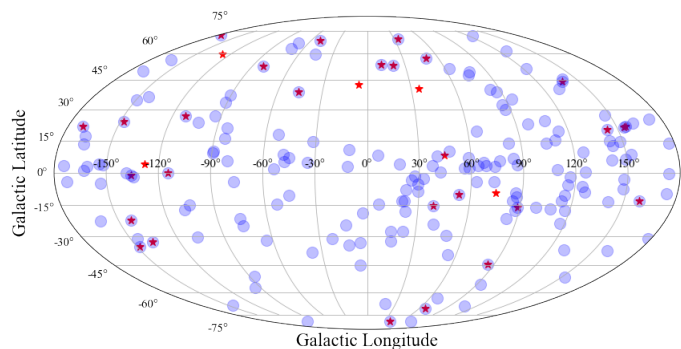


Fig. 1. Position of the stars in our sample. The circles represent the stars part of the DEATHSTAR sample while the red stars show the AGB stars in the VLBI sample.

spectra. They were collected from Stephenson (1984) and Jorissen & Knapp (1998). About $\sim 93\%$ of the stars in the DEATHSTAR sample have their parallaxes measured by *Gaia* and are in eDR3 and DR3.

3. Correcting the *Gaia* parallaxes

3.1. VLBI parallax measurement

Long-period variables, including AGB stars, can have strong and compact maser emission (e.g. OH, SiO, H₂O masers) that can be tracked to measure parallaxes (e.g. Vlemmings et al. 2002, 2003; Vlemmings & van Langevelde 2007; Nyu et al. 2011; Kamezaki et al. 2016a; Nakagawa et al. 2014; Chibueze et al. 2020; VERA Collaboration et al. 2020). Parallax measurements with VLBI make use of the phase-referencing method where the maser-emitting source is monitored once per month, for example, simultaneously with a bright reference source over the course of one or more years. The parallax is obtained by fitting the offsets in the position of the maser spot as a function of time. The errors on the measured parallaxes include both systematic, such as atmospheric calibration errors, and thermal errors. The main assumption needed to measure the parallaxes with this technique is on the motion of the maser features with respect to the star. For some sources, a maser that occurs in the outer CSE on the direct line of sight to the star amplifies the radio emission from the stellar radiophotosphere, producing the so-called amplified stellar image. In this case, the motion of the maser directly reflects the motion of the AGB star (Vlemmings et al. 2003). Alternatively, one can assume that the maser features follow linear motions in the shell, as in Vlemmings & van Langevelde (2007). In most cases, the motions of maser spots are small (Vlemmings et al. 2003), thus parallaxes measured with VLBI astrometry are highly accurate. For AGB stars in particular, parallaxes obtained from maser observations are more robust than *Gaia* DR3 parallaxes, which are measured in the optical, as they are not affected by dust obscuration. Furthermore, tracking the maser spots overcomes problems related to stellar variability (e.g. Vlemmings et al. 2003; Vlemmings & van Langevelde 2007). Therefore, the more precise VLBI parallaxes can be used to calibrate the *Gaia* DR3 parallaxes and their uncertainties.

¹ www.astro.uu.se/deathstar

² Variable star index; <https://www.aavso.org/vsx/index.php>

Table 1. Properties of the VLBI sources.

Source	Var	P [days]	ϖ_{VLBI} [mas]	$\sigma_{\varpi}^{\text{VLBI}}$ [mas]	ϖ_{DR3} [mas]	$\sigma_{\varpi}^{\text{DR3}}$ [mas]	excess noise [mas]	RUWE	G [mag]	G_{BP} [mag]	G_{RP} [mag]
AP Lyn	M	730	2.00	0.04	2.02	0.12	1.07	1.60	8.68	13.88	6.94
BX Cam	M	486	1.73	0.03	1.76	0.1	1.06	1.4	10.06	16.04	8.37
BX Eri	M	165	2.12	0.1	2.35	0.06	0.53	1.0	6.77	10.1	5.15
FV Boo	SR	313	0.97	0.06	1.01	0.09	0.79	1.4	10.59	15.05	8.86
HS UMa	LB	-	2.82	0.1	3.2	0.1	0.56	1.4	6.08	9.34	4.49
HU Pup	SRa	238	0.31	0.04	0.29	0.03	0.28	1.3	7.02	8.88	5.74
NSV 17351	M	680	0.25	0.01	0.09	0.15	1.31	2.1	12.57	18.2	11.15
OZ Gem	M	598	0.81	0.04	0.46	0.33	2.41	3.3	13.84	18.48	11.95
QX Pup	M	551	0.61	0.03	0.03	0.16	0.0	1.0	18.27	18.68	16.34
R Aqr	M	387	4.59	0.24	2.59	0.33	1.33	2.0	6.71	10.76	4.87
R Cnc	M	357	3.84	0.29	3.94	0.18	1.13	2.0	6.53	10.68	4.92
R Hya	M	380	7.93	0.18	6.74	0.46	2.61	2.9	3.15	6.84	2.33
R Peg	M	378.1	2.76	0.28	2.63	0.12	0.63	1.3	7.6	12.06	5.84
R UMa	M	301.62	1.97	0.05	1.75	0.09	0.71	1.0	7.92	11.61	6.41
RR Aql	M	396.1	2.44	0.07	1.95	0.11	0.84	1.5	8.43	13.15	6.81
RT Vir	SRb	157.9	4.42	0.13	4.14	0.23	1.33	1.3	5.09	8.42	3.52
RW Lep	SRa	149.9	1.62	0.16	2.54	0.08	0.64	1.2	7.17	10.74	5.56
RX Boo	SRb	158	7.31	0.5	6.42	0.23	1.59	1.7	4.37	7.84	2.94
S CrB	M	360.26	2.39	0.17	2.6	0.11	1.09	1.6	6.86	11.19	5.09
S Crt	SRb	155	2.33	0.13	2.06	0.1	0.63	1.4	6.34	9.26	4.78
S Ser	M	371.84	1.25	0.04	0.77	0.13	1.12	3.5	8.41	12.36	6.74
SV Peg	SRb	144.6	3.0	0.06	2.59	0.17	1.2	4.4	5.67	9.04	4.07
SY Aql	M	355.92	1.1	0.07	1.07	0.09	0.81	1.4	9.36	13.67	7.83
SY Scl	M	411	0.75	0.03	0.52	0.12	0.93	2.0	9.74	13.98	7.96
T Lep	M	372	3.06	0.04	3.09	0.1	0.95	2.3	6.91	11.32	5.24
U Her	M	404	3.76	0.27	2.36	0.08	0.67	1.3	6.91	11.12	5.21
U Lyn	M	433.6	1.27	0.06	1.01	0.08	0.61	1.3	8.49	12.84	6.75
UX Cyg	M	569	0.54	0.06	0.7	0.09	1.0	3.0	10.0	14.39	8.47
V637 Per	SR	-	0.94	0.02	0.85	0.1	0.73	1.3	9.04	12.43	7.46
V837 Her	M	514	1.09	0.01	0.18	0.10	0.85	1.2	10.74	16.55	9.05
W Leo	M	391.75	1.03	0.02	0.88	0.11	0.65	1.0	9.83	14.48	8.21
X Hya	M	299.5	2.07	0.05	2.53	0.11	0.68	1.6	7.88	11.66	5.88
Y Lib	M	277	0.86	0.05	0.83	0.08	0.6	1.6	9.76	13.68	8.09

Var: variability type.

M: Mira, SRa/b: semi-regular a or b.

LP: long period variable, U: unknown.

P : period from VSX²(Watson et al. 2021).

3.2. VLBI sample

To calibrate the *Gaia* DR3 parallaxes, we used existing VLBI parallax measurements of maser-emitting oxygen-rich AGB stars in the literature. We first considered the AGB stars in the sample of the VLBI Exploration of Radio Astrometry or VERA³ catalogue (VERA Collaboration et al. 2020). The VERA survey consists of four 20-m radio telescopes targeting H₂O and SiO maser emission at 22 and 43 GHz, yielding maps with an angular resolution reaching up to 1.2 and 0.7 mas, respectively. The VERA catalogue comprises 99 objects out of which 29 are labelled as AGB stars. Out of these, 3 are proto-planetary nebulae/post-AGB stars and 26 are AGB stars, according to the SIMBAD⁴ database. Three additional VERA sources

were published by Chibueze et al. (2020) and Sun et al. (2022). We also considered the maser-emitting AGB stars in the sample presented in Xu et al. (2019) which was compiled from the results of Vlemmings et al. (2003); Kurayama et al. (2005); Vlemmings & van Langevelde (2007), and Zhang et al. (2017). Out of the 13 sources labelled as AGB stars that do not overlap with the VERA sample in the Xu et al. (2019) sample, 6 are actually known supergiants or hypergiants. Moreover, as our aim was to use the VLBI parallaxes as calibrators for the *Gaia* DR3 parallaxes, we disregarded the sources whose VLBI parallax measurements have a signal-to-noise ratio lower than 5. This is the case for BW Cam, R Cas, and W Hya. Therefore, our VLBI sample consists of an aggregate of 33 maser-emitting AGB stars (28 VERA, 5 from Xu et al. 2019).

The Galactic distribution and the overlap of the DEATH-STAR and the VLBI samples are shown in Fig. 1. The properties of the VLBI sources are listed in Table 1. We retrieved the *Gaia*

³ <https://www.miz.nao.ac.jp/veraserver/related/index-e.html>

⁴ <http://simbad.u-strasbg.fr/simbad/>

DR3 parallaxes and parallax uncertainties, ϖ_{DR3} and $\sigma_{\varpi}^{\text{DR3}}$, respectively, for the sources in the VLBI sample, along with their G , G_{BP} , and G_{RP} magnitudes from the *Gaia* online archive⁵. The astrometric excess noise and the RUWE (re-normalised unit weight error), also taken from the *Gaia* archive, measure discrepancies in photocentric motions, and therefore, quantify the goodness-of-fit of the *Gaia* DR3 astrometric data. The period P and variability of the stars were taken from the Variable Star Index or VSX online tool (Watson et al. 2021).

3.3. *Gaia* DR3 parallax

3.3.1. G magnitude and colour

We first investigated the dependence of the *Gaia* DR3 parallax uncertainties and the parameters that represent the goodness-of-fit of the astrometric data on the G magnitude, and the colour $G_{\text{BP}} - G_{\text{RP}}$ for the sources in the VLBI sample (Fig. 2) and in the DEATHSTAR sample (Fig. 3). It is apparent in Figs. 2 and 3 that the fainter the star, the redder it is and the smaller its parallax, as expected. However, this behaviour breaks down for the faintest stars ($G \geq 12$ mag). The nominal fractional parallax error seems mostly reasonable (below 20%) for sources brighter than $G = 8$ mag, but shows a slight increase between 8 and 12 G magnitudes. For the three faintest sources in the VLBI sample, the standard *Gaia* DR3 parallax error is larger than 75% (Fig. 2), while a wider scatter is observed for the faintest stars in the DEATHSTAR sample (Fig. 3). The astrometric excess noise worsens with G magnitude, with an obvious general increase above $G = 8$ mag. It does not show a strong dependence on the colour. The RUWE does not strongly correlate with neither the colour nor the G magnitude.

We divided the sources in the VLBI and the DEATHSTAR samples into three categories according to their G magnitudes: (1) $G < 8$, (2) $8 \leq G < 12$, and (3) $G \geq 12$ mag. This division is mainly based on the behaviour of their parallax fractional error and the goodness of the *Gaia* DR3 astrometric measurements measured by their astrometric excess noise, as seen in Figs. 2 and 3.

3.3.2. Zero-point offset and error inflation factor

Figure 4 shows a direct comparison of the VLBI and the *Gaia* DR3 parallaxes, ϖ_{VLBI} and ϖ_{DR3} , respectively, for the sources in the VLBI sample. A rather good agreement is observed for the stars with parallaxes lower than 4 mas, with increasing scatter and uncertainties at higher parallax values, corresponding to the brightest sources, along both axes. Figure 4 also shows that the nominal noise of the *Gaia* DR3 parallaxes, $\sigma_{\varpi}^{\text{DR3}}$, is smaller than the VLBI parallax uncertainties $\sigma_{\varpi}^{\text{VLBI}}$. However, the uncertainties of the parallaxes measured with *Gaia* are known to be underestimated, especially for variable objects such as AGB stars. The previously mentioned astrometric excess noise was introduced in DR2 as the extra uncertainty that must be added in quadrature to the nominal noise to obtain a statistically acceptable astrometric solution for *Gaia* DR2 measurements (Lindgren et al. 2012). A comparative study was conducted by van Langevelde et al. (2018) using *Gaia* DR2 and VLBI measurements for a number of sources including Mira variables, pre-main sequence stars, and binary pulsars. van Langevelde et al. (2018) attribute the large residual in the *Gaia* parallaxes to the effects of the properties, such as the colour and

surface brightness distribution, of the AGB stars in their sample. Their study confirms that adding the astrometric excess noise of the *Gaia* measurements to the nominal noise equalises the *Gaia* DR2 parallaxes with the more robust VLBI measurements.

In this work, we calibrated the *Gaia* DR3 parallaxes for AGB stars using the sample of VLBI sources described in Sect. 3.2, which is larger than, and includes, the sample of van Langevelde et al. (2018). To that end, we normalised the distribution of the difference $\Delta\varpi = \varpi_{\text{DR3}} - \varpi_{\text{VLBI}}$ by the sum of the uncertainties in quadrature. We then adjusted the *Gaia* DR3 uncertainties until that normalised statistical distribution of the parallax difference had the properties of a standard Gaussian, with 0 mean and a standard deviation of 1, as illustrated by Fig. 5. This was done for the three categories described in Sect. 3.3.1. The correction factor to be applied to the *Gaia* DR3 parallax errors or the error inflation factor (*EIF*), that is,

$$\sigma_{\varpi,\text{tot}}^{\text{cor}} = \sqrt{(\text{EIF} \cdot \sigma_{\varpi}^{\text{DR3}})^2 + (\sigma_{\varpi}^{\text{VLBI}})^2} \text{ mas}, \quad (1)$$

and the zero-point offset (*ZPO*) of the parallax,

$$\varpi_{\text{DR3}}^{\text{cor}} = \varpi_{\text{DR3}} - \text{ZPO} \text{ mas}, \quad (2)$$

are given in Table 2. Figure 5 also shows the cases where no correction was applied to the total error, that is, $\sigma_{\varpi,\text{tot}} = \sqrt{(\sigma_{\varpi}^{\text{DR3}})^2 + (\sigma_{\varpi}^{\text{VLBI}})^2}$ mas, and where the astrometric excess noise was added to the *Gaia* standard errors, $\sigma_{\varpi,\text{tot}} = \sqrt{(\sigma_{\varpi}^{\text{DR3}})^2 + \sigma_{\text{excess noise}}^2 + (\sigma_{\varpi}^{\text{VLBI}})^2}$ mas, as in van Langevelde et al. (2018). Since the distribution of the parallax difference shown in Fig. 5 was normalised by the total error, only taking into account the standard *Gaia* DR3 uncertainties without any correction led to an underestimation of the total error, resulting in a parallax difference distribution broader than the standard Gaussian for the sources brighter than $G = 12$ mag. However, including the astrometric excess noise parameter to the total uncertainty of the *Gaia* DR3 parallax of these bright sources overestimated the total error, which led to a narrower parallax difference distribution ($\Delta\varpi/\sigma_{\varpi,\text{tot}}$), as indicated by the blue line in Fig. 4. Furthermore, Fig. 6 shows that the astrometric excess noise parameter for *Gaia* DR3 is larger than for the DR2 parallaxes for the VLBI sources. The median value of the ratio of astrometric excess noises DR3/DR2 for the VLBI sample is 1.22, and 76% of the sources have an astrometric excess noise DR3/DR2 ratio larger than 1. For the DEATHSTAR sample, close to 60% of the sources have an astrometric excess noise higher in DR3 than in DR2.

Our results show that the parallax errors of the brightest sources ($G < 8$) are dramatically underestimated, by more than a factor of 5. For sources between 8 and 12 G mag, the nominal errors are larger, so a relatively smaller correction was needed. For the faintest stars, the nominal *Gaia* DR3 parallax errors are, in principle, already very large, so little correction was needed on the *Gaia* DR3 parallax errors. For some of these faint sources, the *Gaia* DR3 parallax errors are so large that they would have needed to be reduced to recover the corresponding VLBI parallaxes. Distances obtained with parallaxes with such large errors are likely to be very uncertain (see Sect. 4). Only 3 VLBI sources are fainter than 18 mag, which is a too small sample to obtain statistically significant results. Therefore, we did not apply any correction to the faintest stars ($G \geq 12$ mag). When considering the VLBI sample as a whole (33 stars), we obtained a constant *EIF* of ~ 4 . However, it is clear from Figs. 2–3 and Table 2 that not all sources require the same correction factor, so a constant *EIF* is not suitable.

⁵ <https://gea.esac.esa.int/archive/>

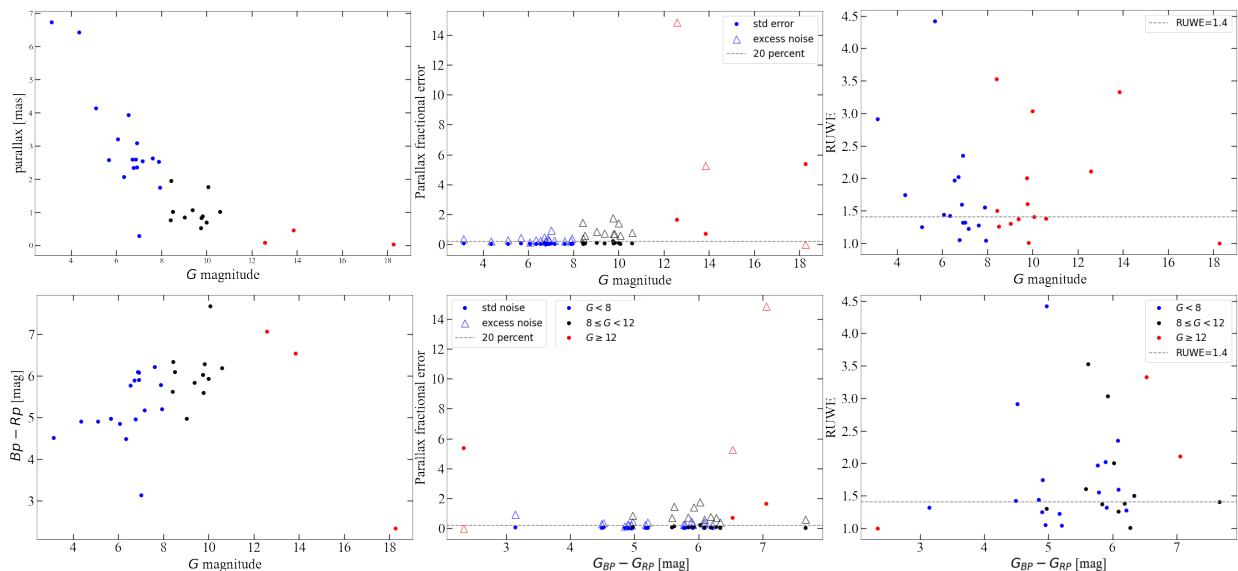


Fig. 2. Dependence of the standard noise, the astrometric excess noise, and the RUWE of the *Gaia* DR3 parallax on the G magnitude and the colour $G_{BP} - G_{RP}$ for the sources in the VLBI sample.

Table 2. *Gaia* DR3 parallax zero-point offset (ZPO) and error inflation factor (EIF).

G	N_{VLBI}	ZPO	EIF
< 8	17	-0.077 ± 0.004	5.44 ± 0.11
$\geq 8 \ \& \ < 12$	13	-0.174 ± 0.006	$2.74^{+0.04}_{-0.05}$
all**	33	$-0.131^{+0.016}_{-0.015}$	$4.20^{+0.10}_{-0.11}$

N_{VLBI} : number of VLBI sources

** all G included, constant ZPO and EIF .

Using the properties of resolved binaries to calibrate the *Gaia* eDR3 parallaxes, El-Badry et al. (2021) found that the published *Gaia* eDR3 parallax uncertainties are underestimated by ~ 30 to 80% for bright red sources ($G < 12$ mag), but are generally more reliable for fainter sources ($G \geq 18$ mag), which is in agreement with our findings on AGB stars. The dependence of the parallax ZPO of the *Gaia* eDR3 parallaxes on the sky position and magnitude are discussed in detail in Lindegren et al. (2021) and Groenewegen (2021), for instance, using samples of quasi-stellar objects and wide binaries. The zero-point offsets that we obtained for AGB stars, listed in Table 2, are much larger, in absolute value, than the global eDR3 zero-point offset of -0.028 mas derived by Ren et al. (2021), and of -0.039 mas by Groenewegen (2021).

4. From parallax to distance

The distance r of an object is equal to the inverse of its true parallax ϖ_{True} . Assuming that the measured parallax ϖ is a value taken from a normal distribution around the true parallax $\varpi_{\text{True}} = 1/r$, with a known standard deviation σ_{ϖ} , the likelihood of that measured parallax is given by

$$P(\varpi | r, \sigma_{\varpi}) = \frac{1}{\sqrt{2\pi}\sigma_{\varpi}} \exp\left[-\frac{1}{2\sigma_{\varpi}^2}\left(\varpi - \frac{1}{r}\right)^2\right], \quad (3)$$

where $\sigma_{\varpi} > 0$. Bailer-Jones (2015) showed that determining the distance from a probability distribution over the parallax presents several problems including negative parallaxes, in particular when the fractional error on the parallax is large (Luri et al. 2018).

A better approach is to infer the most probable value of the distance amongst all its possible values from the noisy measured parallax (Bailer-Jones 2015; Astraatmadja & Bailer-Jones 2016a,b; Bailer-Jones et al. 2018, 2021). Such a posterior probability distribution over the distance is the product of the likelihood of the measurement, $P(\varpi | r, \sigma_{\varpi})$, and an appropriate prior information on the distance, $P(r)$. Following Bayes theorem,

$$P(r | \varpi, \sigma_{\varpi}) = \frac{1}{Z} P(\varpi | r, \sigma_{\varpi}) P(r), \quad (4)$$

where Z is a normalisation constant independent of the distance,

$$Z = \int_0^{r_{\text{max}}} P(\varpi | r, \sigma_{\varpi}) P(r) dr. \quad (5)$$

The value of the most probable distance is given by the median of the posterior distribution (Bailer-Jones et al. 2021). The resulting distance uncertainties are asymmetrical because of the non-linear nature of the $1/\varpi$ to r transformation.

The determining factor in this distance inference problem is the fractional error on the parallax. For a parallax fractional error higher than 20% , the posterior over the distance is highly asymmetrical (Bailer-Jones 2015). This effect worsens with increasing fractional error which results in a non-negligible increase in the value of the derived distance and its uncertainties, and therefore leads to less reliable distances. About 63% of the sources published in eDR3 have parallax fractional errors larger than 20% (Bailer-Jones et al. 2021).

We calculated the posterior distribution over the distance for the sources in the VLBI and the DEATHSTAR samples. In that process, the choice of the prior was paramount. The

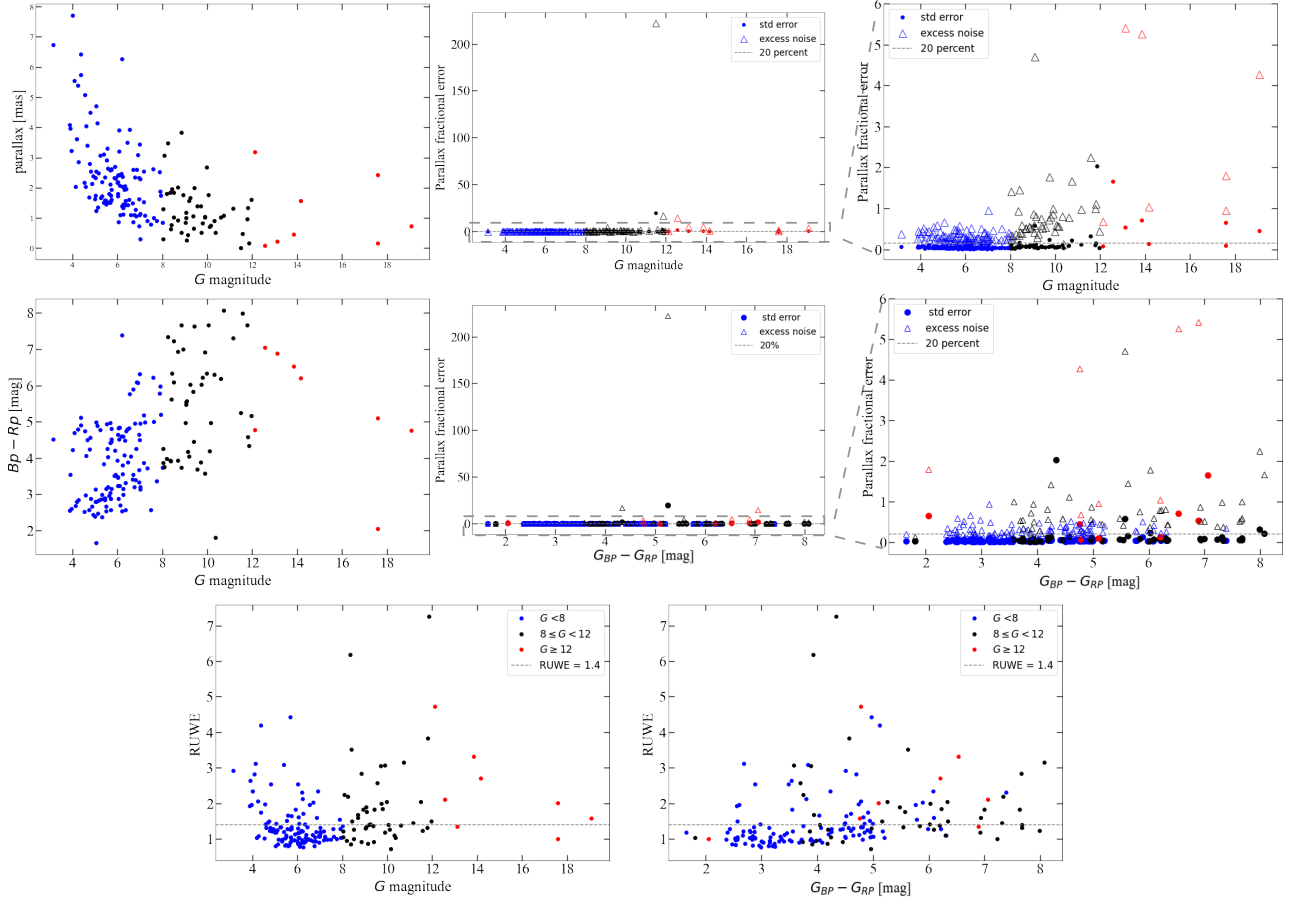


Fig. 3. Dependence of the standard noise, the astrometric excess noise, and the RUWE of the *Gaia* DR3 parallax on the *G* magnitude and the colour $G_{BP} - G_{RP}$ for the sources in the DEATHSTAR sample.

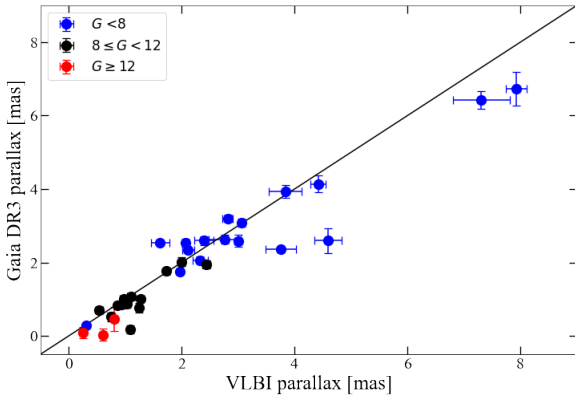


Fig. 4. Comparison between the VLBI and *Gaia* DR3 parallaxes. The solid line represents the 1-to-1 relation.

more assumptions are introduced into the prior, the more model-dependent the resulting distances are, especially when the errors involved are large. Therefore one should choose a prior that closely represents the expected data. To this end, we tested four different priors: a uniform distribution (UD) prior defined

in Bailer-Jones (2015) as

$$P_{UD} = \begin{cases} \frac{1}{r_{\max}}, & \text{if } 0 < r < r_{\max}; \\ 0, & \text{otherwise} \end{cases}; \quad (6)$$

a uniform space distribution (USD) prior that is corrected for increasing volume, following the definition given by Bailer-Jones (2015)

$$P_{USD} = \begin{cases} \frac{3r^2}{r_{\max}^3}, & \text{if } 0 < r < r_{\max}; \\ 0, & \text{otherwise.} \end{cases}; \quad (7)$$

an exponentially decreasing space distribution (EDSD) prior that exponentially decreases to 0 as the distance increases, given by

$$P_{EDSD} = \begin{cases} \frac{r^2}{2L^3} e^{-(r/L)}, & \text{if } r > 0 \\ 0, & \text{otherwise} \end{cases}; \quad (8)$$

(Bailer-Jones 2015), with $L = 250$ pc; and a more realistic prior that describes the Galactic distribution of AGB stars (AGB prior). According to Jura & Kleinmann (1990, 1992), the distribution of AGB stars in the Galaxy follows a vertical scale height up to $Z_0 = 240$ pc, and a disc scale length set at R_0 of 3500 pc. The AGB prior is also corrected for increasing volume, so that

$$P_{AGB} = \begin{cases} \frac{3r^2}{r_{\max}^3} e^{-(|z|/Z_0)} e^{-(R_{\text{Gal}}/R_0)}, & \text{if } 0 < r < r_{\max} \\ 0, & \text{otherwise} \end{cases}, \quad (9)$$

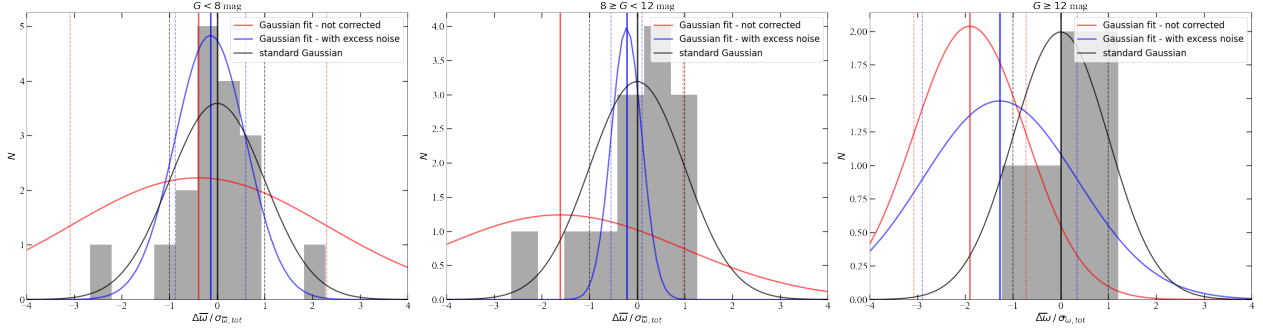


Fig. 5. Gaussian fittings of the parallax difference distribution $\Delta\omega / \sigma_{\omega,tot}$ for the three G magnitude categories. The distributions were normalised by the quadratically summed errors of the VLBI error with either: the DR3 parallax standard error without any correction ($\sigma_{\omega,tot} = \sqrt{(\sigma_{\omega}^{DR3})^2 + (\sigma_{\omega}^{VLBI})^2}$, red line), or with the astrometric excess noise ($\sigma_{\omega,tot} = \sqrt{(\sigma_{\omega}^{DR3})^2 + \sigma_{\text{excess noise}}^2 + (\sigma_{\omega}^{VLBI})^2}$, blue line), or with the DR3 parallax standard error inflated by the EIF listed in Table 2 and the parallax corrected for the ZPO ($\sigma_{\omega,tot} = \sqrt{(EIF \cdot \sigma_{\omega}^{DR3})^2 + (\sigma_{\omega}^{VLBI})^2}$, black line representing a standard Gaussian). The dashed lines correspond to the respective standard deviations of the Gaussians, while the solid straight lines show the mean values. The offset of the mean value with respect to 0 is a measure of the ZPO.

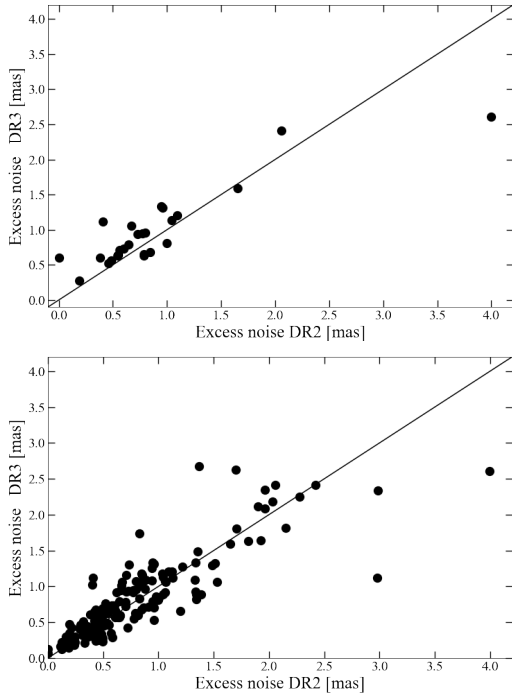


Fig. 6. Comparison between the astrometric excess noise of Gaia DR2 and DR3 for the VLBI sample (top) and the DEATHSTAR sample (bottom). The solid lines show the 1-to-1 relation.

where R_{Gal} is the distance to the Galactic centre and z the height above the Galactic plane.

By checking the 2MASS K -band magnitudes of our sample, we found an apparent K -band limit of 3.2 mag. Assuming that the tip of the AGB is at $V = -2$ for a solar-mass star, and taking an average of $(V - K) = 8$ from theoretical estimates (Bladh et al. 2013), we obtained a maximum distance estimate

of 4400 pc. We therefore limited the allowed distances r_{max} for the sources in our sample to $r_{\text{max}} = 4500$ pc.

The Galactic distribution that defines the AGB prior used in this work, based on the findings of Jura & Kleinmann (1992), is in agreement with the Galactic distribution derived by Ishihara et al. (2011) who investigated the difference between the distribution of AGB stars in the Milky Way for the M- and C-type stars. They found a concentration of oxygen-rich stars toward the Galactic centre, with a density decreasing with Galactocentric distance, and a rather uniform distribution within about 8 kpc of the Sun for carbon-rich AGB stars. Jackson et al. (2002) found a distribution that follows a vertical scale height up to 300 pc and a constant number of AGB stars in the radial direction, up to 5 kpc, above which the density decreases exponentially with a scale length of 1.6 kpc, extending to ~ 12 kpc. The scale length that we adopted in the AGB prior is consistent with the results of both studies. Varying the scale height Z_0 or scale length R_0 did not significantly change the derived distances (less than 10 % of deviation). The only parameter that affected the derived distances, mostly for the farthest stars, was the maximum allowed distance r_{max} . Lowering its value led to an increase in the number of sources whose distances were stuck at that upper limit because the posteriors could not reach convergence. Increasing r_{max} to 5000 pc only changed the distance of two of the stars in the DEATHSTAR sample, putting them at that new upper limit, implying that the distances to these sources are very poorly constrained.

We find that parallax fractional errors larger than $\sim 18\%$ already lead to notable errors in the derived distances ($\geq 20\%$ distance error with the AGB prior) for some of the sources. More significant uncertainties are associated with parallax fractional errors greater than the previously mentioned 20 % cutoff. About 85 % of the VLBI sample have a *Gaia* DR3 parallax fractional error smaller than 0.2 when considering the standard error, but that number decreases to $\sim 35\%$ after applying the correction to the *Gaia* DR3 parallaxes derived in Sect. 3. In the case of the DEATHSTAR sample, 94 % of the sources have a fractional parallax error lower than 20 % before correction, which decreases

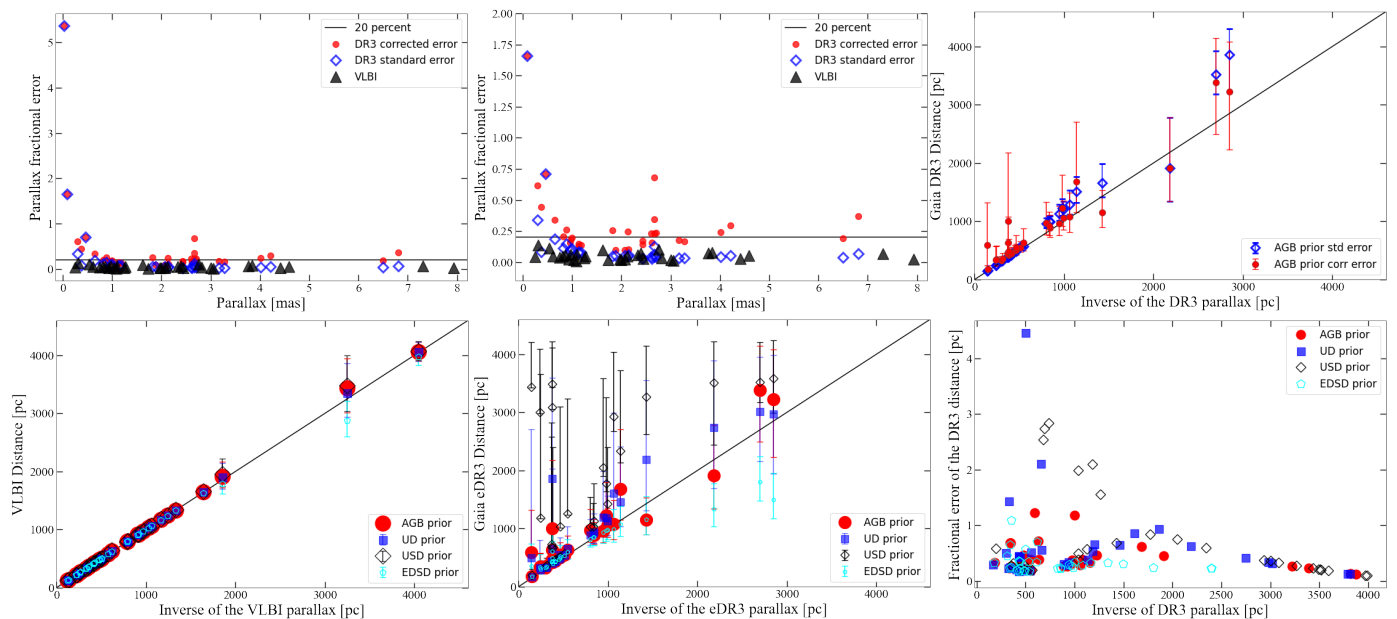


Fig. 7. *Gaia* DR3 and VLBI parallaxes with the corresponding distances for the VLBI sample. **Top panels:** Fractional errors of the VLBI (black full triangles) and *Gaia* DR3 parallaxes using the standard nominal error (blue open diamond) and with the corrected errors (red full circles) for the VLBI sources. The plot in the middle is a zoomed version of the plot on its left. The plot on the right compares the distances derived with *Gaia* DR3 parallaxes with the corrected (red) and the standard errors (blue). **Bottom panels:** Distances derived using the four priors for the VLBI sources using the VLBI parallaxes (left) and the corrected *Gaia* DR3 parallaxes (middle). The solid lines represent the 1-to-1 relation. The plot at the bottom-right shows the fractional error on the derived distances.

to $\sim 52\%$ after correcting the errors on the DR3 parallaxes (see Table A.1).

As expected, the distances derived with the VLBI parallaxes are mostly unchanged with the four priors due to the low measurement uncertainties, as illustrated in Fig. 7. The fractional errors on the VLBI parallaxes are lower than 20% for almost all the sources. In such cases, the posterior distribution is dominated by the likelihood of the data, and the choice of prior does not change the derived distances. The uncertainties on the derived distances are also mostly smaller than 20%, showing their high level of reliability.

The distances derived with the corrected *Gaia* DR3 parallaxes are strongly dependent on the prior, as the latter dominates the posterior at large parallax fractional errors. The effects of the value of the parallax fractional errors on the derived distances are illustrated in Figs. 7 and 8, showing comparisons between the *Gaia* DR3 distances obtained with the different priors, and using the standard and the corrected errors of the *Gaia* DR3 parallaxes for the sources in the VLBI (Fig. 7) and the DEATHSTAR samples (Fig. 8).

In the following, we focus on the distances estimated using the AGB prior, as it is more informative and realistic. It is also more sensitive than the other priors we tested because of the larger number of parameters in it. The larger the uncertainties, the higher the probability for the true parallax to be smaller than the measured parallax. As a result, our estimate of the true distance increases. This is known as the Lutz–Kelker bias (Lutz & Kelker 1973). The fractional error on the measurements and the sensitivity of the prior determine how bad the effects are, which means that even nearby objects can be affected. The large errors on the parallaxes lead to significant errors on the derived dis-

tances, making them unreliable. Using the corrected *Gaia* DR3 parallaxes and the AGB prior, we found that about 46% of the sources in the DEATHSTAR sample have distance fractional errors larger than 25%, while more than 15% of them have distance fractional errors greater than 50%. When the prior and/or the posterior distribution did not converge or when the uncertainty on the derived distance was too large, we rejected the derived distance.

5. A new PL relation for Miras

A number of the distances derived with the corrected *Gaia* DR3 parallaxes following the method described in Sect. 4 are highly uncertain for the sources in the DEATHSTAR sample, and thus rejected. Therefore, we turned to a different method to estimate the distances to these sources: the PL relation. We derived a new bolometric PL relation based on the VLBI distances of the Mira variables in the VLBI sample.

The luminosity of the sources in the VLBI sample were obtained by modelling their spectral energy distributions (SEDs) using the radiative transfer code DUSTY (Ivezic et al. 1999). DUSTY solves the radiative transfer through a dusty environment including dust absorption, emission, and scattering. The details of the SED fitting are given in Appendix B. From the dust modelling, we obtained the effective temperature of the central star, T_{\star} , the dust temperature at the inner radius, T_d , the optical depth at $10\ \mu\text{m}$, τ_{10} , and the bolometric luminosity, L_{\star} , of each source in the VLBI sample. These results are listed in Table 3.

The bolometric magnitude M_{bol} of each star was calculated (assuming $M_{\text{bol},\odot}=4.74$) and correlated with the variability period which was taken either from the GCVS (Samus' et al.

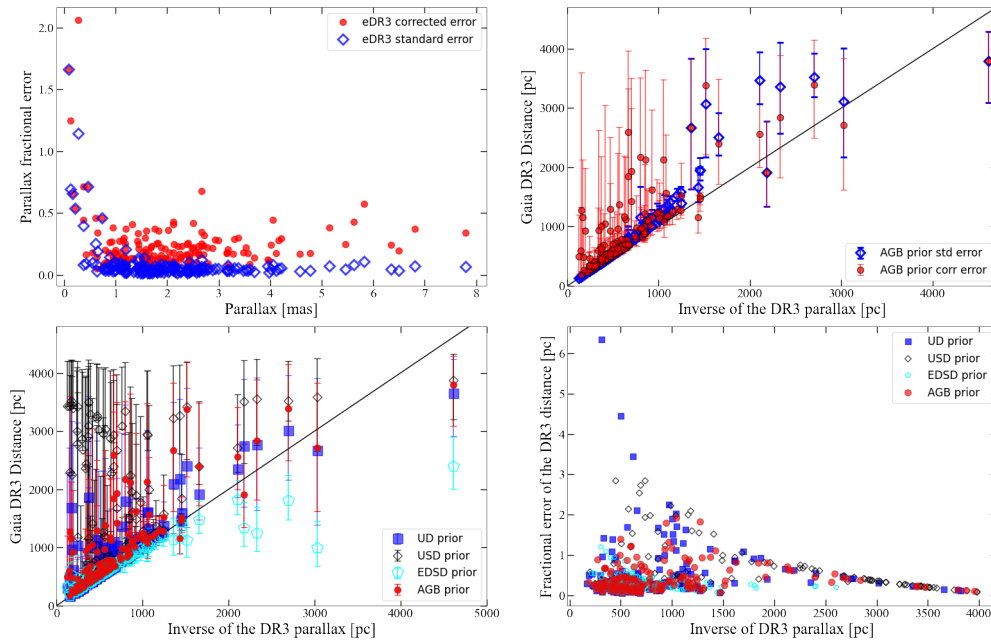


Fig. 8. *Gaia* DR3 parallaxes and the corresponding distances for the DEATHSTAR sample. **Top panels:** Fractional errors of the *Gaia* DR3 parallaxes using the standard nominal error (blue open diamond) and with the corrected errors (red full circles) for the DEATHSTAR sources. The right plot compares the distances derived with *Gaia* DR3 parallaxes with the corrected (red) and the standard errors (blue). **Bottom panels:** Distances derived with the four priors for the DEATHSTAR sources using the corrected *Gaia* DR3 parallaxes. The solid lines represent the 1-to-1 relation. The plot on the right shows the fractional error on the corrected *Gaia* DR3 distances.

2017) or the International Variable Star Index (VSX; Watson et al. 2021). We removed from the PL relation derivation the sources that are known or suspected not to behave as regular Mira variables. The OH/IR stars in the VLBI sample were, therefore, excluded from this analysis. These stars lie at the end of the evolution of the AGB and have very high mass-loss rates (Herman et al. 1985). They have been found to consistently lie below the PL relation of typical Miras (van Langevelde et al. 1990; Whitelock et al. 1991). The stars in our VLBI sample labelled as OH/IR in the SIMBAD database are NSV 17351, QX Pup, and SY Aql. In addition, OZ Gem has recently been suspected as being in the process of becoming an OH/IR star (Urago et al. 2020). The study conducted by Chibueze et al. (2020) suggests that AP Lyn could undergo the same process as OZ Gem due to its high mass-loss rate. Finally, we also excluded FV Boo and UX Cyg from the Mira-PL relation determination. Lewis (2002a,b) described FV Boo as a dying OH/IR star, with a mass loss that abruptly switches on and off. Monitoring of FV Boo in the IR over a 20-year span by Kamezaki et al. (2016b) showed that it suffered a temporary but significant dip in its luminosity in 2005. The star UX Cyg stood out in the sample of Mira variables investigated by Etoke & Le Squeren (2000) due to rapid, large changes in the amplitude of the variations of its maser lines, likely linked to an unusually turbulent envelope. Whitelock et al. (2008) excluded UX Cyg from their *K*-band PL relation as they hypothesised it to be either an overtone pulsator or a hot bottom burning candidate.

We used the form of the PL relation introduced by Whitelock et al. (2008) where the zero-point is shifted within the range of typical periods of Mira variables. The resulting PL relation has

a slope of -2.67 ± 1.88 and a zero-point of 2.323 ± 4.832 . The large errors are due to the small sample size. This problem can be solved by using a fixed slope and by keeping the zero point as only free parameter. Using stars in the Large Magellanic Cloud (LMC) and in the Milky Way, Whitelock et al. (2008) showed that, while the zero-point differs for oxygen-rich and carbon stars, the slope of the *K*-band PL relation is nearly invariant. In addition, using a common fixed slope for the Milky Way and the LMC, Whitelock et al. (2008) showed that the zero-point of the *K*-band PL relation for Mira variables in these two different environments were consistent with each other within their uncertainties, implying that the *K*-band PL relation is universal. This property of universality was then extended to the bolometric PL relation by Whitelock et al. (2009), where they determined the distance to the Fornax Galaxy using a bolometric PL relation derived in the LMC. Accordingly, with the assumption that the slope invariance with chemical type is also applicable to the bolometric PL relation, we use the slope of $\rho_{\text{fixed}}^{\text{shift}} = -3.31 \pm 0.24$ derived for C-stars in the LMC by Whitelock et al. (2009). We obtain the PL relation given by

$$M_{\text{bol}} = (-3.31 \pm 0.24) [\log P - 2.5] + (-4.317 \pm 0.060). \quad (10)$$

The zero-point derived in this work for M-type stars reasonably agrees with existing bolometric PL relations for C-stars both in the LMC (Whitelock et al. 2006, 2009) and in the Milky Way (Feast et al. 2006), as seen in Fig. 9. In particular, our PL relation is in excellent agreement with the zero-point of the PL relation of Whitelock et al. (2009). Whitelock et al. (2008, 2009) compared the luminosity obtained from interpolating IR measurements with the luminosity derived from dust modelling using DUSTY (e.g. Matsuura et al. 2007) and concluded that the

Table 3. DUSTY results for the VLBI sources.

Source	r_{VLBI} [pc]	$\sigma_{r,\text{VLBI}}^-$ [pc]	$\sigma_{r,\text{VLBI}}^+$ [pc]	$L_{\star}^{\text{median}}$ [L_{\odot}]	$\sigma_{L_{\star}}^-$ [L_{\odot}]	$\sigma_{L_{\star}}^+$ [L_{\odot}]	T_{\star} [K]	T_{dust} [K]	τ_{10}	PL*
<i>Miras</i>										
AP Lyn	501	10	10	4200	100	200	2900	700	0.28	no
BX Cam	579	10	10	7700	200	200	3000	1000	0.8	yes
FV Boo	1034	60	67	1900	200	200	3000	700	0.3	no
NSV 17351	4064	157	168	25600	1400	1600	3100	1000	1.2	no
OZ Gem	1246	58	63	2500	100	200	2700	600	0.7	no
QX Pup	1652	78	86	1300	100	100	3600	600	5.0	no
R Aqr	220	11	12	8100	600	600	2900	1200	0.14	yes
R Cnc	266	19	22	4800	500	600	2900	600	0.02	yes
R Hya	126	2	3	10300	300	300	3100	1200	0.04	yes
R Peg	374	36	44	4600	600	700	2900	1200	0.11	yes
R UMa	508	12	14	4100	100	200	3000	1200	0.17	yes
RR Aql	411	11	12	3500	100	200	2900	900	0.26	yes
S CrB	424	28	33	8600	900	800	2900	1000	0.07	yes
S Ser	801	25	27	5800	300	300	3000	600	0.04	yes
SY Aql	922	56	64	2800	200	300	3000	700	0.24	no
SY Scl	1330	50	55	5700	300	300	3000	800	0.18	yes
U Her	271	19	21	5800	600	600	2900	1000	0.08	yes
T Lep	327	4	4	6100	200	100	2900	1200	0.06	yes
U Lyn	792	36	39	6000	400	400	3000	900	0.16	yes
UX Cyg	1918	198	250	4000	600	700	3600	600	5.0	no
V837 Per	918	9	8	5400	100	100	3100	1200	1.0	yes
W Leo	971	18	19	6800	200	200	2600	600	0.04	yes
X Hya	484	11	12	3800	100	100	3000	900	0.09	yes
Y Lib	1173	64	73	3200	200	300	3000	700	0.06	yes
<i>SRa</i>										
HU Pup	3437	426	51	29950	3450	3450	2600	600	0.48	no
RW Lep	636	59	72	10300	1400	1500	3000	600	0.02	no
<i>SRb and U</i>										
BX Eri	476	23	25	6500	400	500	3100	600	0.03	no
HS UMa	356	11	13	6100	300	300	3100	600	0.03	no
RT Vir	227	6	7	7400	300	300	3100	600	0.02	no
RX Boo	139	9	11	4700	500	600	3100	600	0.02	no
S Crt	433	23	25	4800	400	400	3200	600	0.01	no
SV Peg	334	7	7	8700	300	400	3100	600	0.02	no
V637 Per	1065	22	23	4500	200	200	3100	600	0.04	no

SRa/b: semi-regular a or b., U: unknown

r_{VLBI} the median distance obtained with the VLBI parallax

$\sigma_{r,\text{VLBI}}^{-/+}$ the lower/upper uncertainties on the VLBI distance.

$L_{\star}^{\text{median}}$ the median luminosity; $\sigma_{L_{\star}}^{-/+}$ the lower/upper uncertainties on the luminosity.

T_{\star} is the stellar temperature; T_{dust} the dust temperature; τ_{10} the optical depth at 10 μm ;

*included in the PL derivation.

latter could be overestimated by up to 50%. On the other hand, bolometric magnitudes in Whitelock et al. (2006, 2009) were estimated by integrating under a spline curve fitted to fluxes at $J, H, K, L, 12,$ and $25 \mu\text{m}$. The curve was extrapolated at the end points to reach zero flux at zero frequency at the short end (long end in wavelength) and by joining the K -band flux with zero flux through a point between the H and K fluxes, which could have underestimated the total luminosity. However, the bolometric magnitude obtained with the PL relation derived in this work is only about 0.046 mag brighter than in Whitelock et al. (2009),

and 0.048 mag fainter than the bolometric magnitudes obtained by Whitelock et al. (2006), on average. Furthermore, although the associated uncertainties are very large because of the small sample size, the PL relation we derived with a non-fixed slope appears, in general, to be consistent with the PL relation derived by Whitelock et al. (2006) (see Fig. 9). As expected, most of the (candidate/dying) OH/IR stars lie below the derived PL relation, with the exception of NSV 17351.

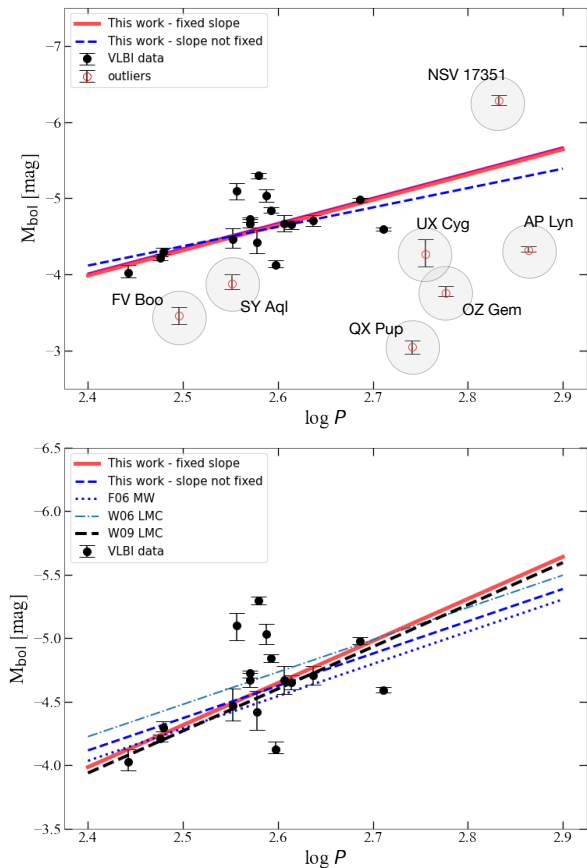


Fig. 9. Derived PL relation for Mira variables. **Top:** Bolometric PL relation based on the luminosity of the Mira variables in the VLBI sample. The red solid line shows the PL relation obtained when using a fixed slope, and the blue dashed line represents the relation obtained when the slope is a free parameter. The sources excluded from the fit are represented by the open symbols. **Bottom:** Comparison between our PL relation with the bolometric PL relations for C-type stars by Feast et al. (2006) in the Milky Way (F06 MW), Whitelock et al. (2006) (W06 LMC), and Whitelock et al. (2009) (W09 LMC) in the LMC.

The universality of the PL relation

As previously mentioned, Whitelock et al. (2008) demonstrated that the PL relation is universal. This was proven by the good agreement between the zero-points of the PL relations in the LMC, the Milky Way, and the Fornax dwarf Galaxy, assuming a common slope. However, recent studies by Urago et al. (2020) and Chibueze et al. (2020) have cast doubt on the universality of the PL relation in environments with different metallicities. Their conclusion of a non-universal PL relation comes from the position of the Galactic oxygen-rich star OZ Gem on the LMC K -band PL diagram. Given its luminosity, chemistry, and high mass-loss rate implied by its very red colour, Urago et al. (2020) concluded that OZ Gem is likely an OH/IR star. Their photometric measurements, however, placed OZ Gem on the region for C-stars on the K -band PL relation in the LMC, below the line for M-type stars (see their fig. 9). Our results, show that OZ Gem also lies below the bolometric PL relation for Mira variables in the Milky Way (see Fig. 9). This corroborates the results of Urago et al. (2020) on the OH/IR nature of this source,

as OH/IR stars tend to have low luminosity for their relatively long period (e.g. fig. 10 in Whitelock et al. 1991) compared to typical Miras. They are also expected to be less luminous in the K -band because of dust obscuration from their thick CSE. In other words, OZ Gem is an outlier even amongst the Mira variables in the Milky Way and its position in the (K -band or bolometric) PL relation does not represent the general trend for the typical Mira variables in the Galaxy. This interpretation, therefore, does not invalidate the universality of the PL relation for regular Miras. However, the absence of typical oxygen-rich Miras at longer periods (> 600 days) is apparent in Fig. 9, as they are expected to be either brighter due to hot bottom burning, or fainter due to high mass-loss rates (e.g. OH/IR stars). There is, however, no such gap at longer periods in the K -band PL relation of oxygen-rich stars in the LMC. The apparent absence of regular oxygen-rich Miras at longer periods in the Milky Way could indicate that the universality of the PL relation with metallicity breaks down at long periods for oxygen-rich Miras.

6. A new distance catalogue

In this section, we present a new distance catalogue for the ~ 200 sources in the DEATHSTAR sample, based on our results in Sects. 3, 4, and 5, and using alternative methods in the literature when applicable, as described below. Table C.1 gives the distances and the associated uncertainties for the nearby AGB stars in the DEATHSTAR sample. The displayed distances are estimated using the following methods.

For the AGB stars in the VLBI sample, we estimated the distances and their errors using the VLBI parallaxes (Type = V in Table C.1), following the Bayesian approach using the AGB prior described in Sect. 4. The corresponding distances have fractional errors within 25%. For the sources outside the VLBI sample that have a corrected *Gaia* DR3 parallax fractional error below 15%, the best distance estimate listed in Table C.1 is the *Gaia* DR3 distance obtained with the AGB prior (Type = G_{AGB}). For sources with a corrected *Gaia* DR3 parallax fractional error between 15 and 20%, we checked if the fractional error on the distance derived using the Bayesian approach with the AGB prior is within 25%. If that condition was fulfilled, the distance in Table C.1 is the *Gaia* DR3 distance with AGB prior (Type = G_{AGB}). Otherwise, the distance was determined using a PL relation, provided that the source had a known period and variability type. The PL relation derived in Sect. 5,

$$M_{bol} = (-3.31 \pm 0.24) [\log P - 2.5] + (-4.317 \pm 0.060),$$

was used to derive the luminosity of the Mira variables (Type = PL(M) in Table C.1). We then performed radiative transfer modelling of the stellar and dust emission, as in Sect. 5, to determine their distances. The details of the dust modelling are given in Appendix B. It is important to note that this PL relation was derived using Mira variables with periods between 277 and 514 days, so the distances for the sources outside this range derived with this relation (Type = PL(M_{out})) can be less reliable. However, given the good agreement between our PL relation and existing PL relations for Miras that are valid within a wider period range, $\sim 160 - 930$ days for Feast et al. (2006), for instance, using our PL relation for sources within that wider range of periods is a reasonable first approximation.

For semi-regulars (SRs), we used the PL relation from Knapp et al. (2003) given by

$$M_K = -1.34(\pm 0.06) \log P - 4.5(\pm 0.35)$$

to estimate the absolute magnitudes of the sources in the K -band. The distance was obtained using the distance modulus relation (Type = PL(SRa/b) in Table C.1). The apparent magnitude in the K -band was retrieved from the VSX online search tool (Watson et al. 2021). Interstellar extinction in the K band is expected to be low. For the sources in our sample that are also in Knapp et al. (2003) or Whitelock et al. (2008), we used the A_K coefficients calculated by Knapp et al. (2003) or the A_V (lower limits) in Whitelock et al. (2008) for these individual sources to correct for reddening. Otherwise, we assumed a value of $A_K = 0.02$ mag, representing the mean value of the A_K distribution in Knapp et al. (2003). The use of a single PL relation for SRs is motivated in the literature by the fact that they are possible progenitors of Mira variables, so some sort of similarity in their behaviour is expected (Feast & Whitelock 2000). The PL relation for SRs by Knapp et al. (2003) that we used here is in good agreement with the relation derived by Yeşilyaprak & Aslan (2004) for SRs, within their respective uncertainties. However, as SRs, SRBs in particular, are less regular and have lower amplitude, their pulsation behaviour is less well-understood than Mira variables, and their period and luminosity show a weaker correlation. In addition, studies such as Soszyński et al. (2013) showed that SRs can have more than one pulsation period and lie on different PL sequences. Therefore, the reliability of the distances derived with this method can be arguable. More recently, Trabucchi et al. (2021) investigated the suitability of SRs as distance indicators and found that a subgroup of SRs follows the same sequence as Mira variables in the PL diagram. However, they concluded that long-time series are necessary to properly classify SRs according to their pulsation periods. The study of the variability of SRs is beyond the scope of this paper. Finally, for the remaining sources in the DEATHSTAR sample with corrected *Gaia* DR3 parallax fractional error larger than 20 %, we estimated the distance with a PL relation, depending on the variability type, as described above.

We note that the distances presented in this catalogue were derived in a systematic way for the whole DEATHSTAR sample. For some sources, however, independent and more accurate source-specific distances obtained with the phase-lag method are available in the literature. This is the case, for example, for IRC+10216 (123 ± 14 pc; Groenewegen et al. 2012), R Scl (361 ± 44 pc; Maercker et al. 2018), and OH/IR stars (e.g. Herman et al. 1985; Engels et al. 2015; Etoaka et al. 2018). Our distance of 408^{+42}_{-34} pc for R Scl agrees rather well with its phase-lag distance. The distance of 190 ± 20 pc that we derived for IRC+10216 with our PL relation for Miras is consistent within 3σ with its distance derived by Groenewegen et al. (2012), but the error is, nonetheless, relatively large. This can be due to the fact that the period of IRC+10216 lies outside the period range with which our PL relation was derived. This shows that one should be careful when using the PL(M_{out}) distances in Table C.1, as the displayed errors do not account for uncertainties related to the longer/shorter periods of these sources.

Comparing the corrected *Gaia* DR3 and the PL distances

We considered the sources that have 'good' *Gaia* DR3 distances, which are distances with fractional errors below 25 %. For comparison purposes, we also derived alternative distances for these same sources, using either the PL relation that we developed in Sect. 5 for the Miras, or the PL relation by Knapp et al. (2003) for the SRs. Figure 10 shows that, for the Miras, the distances derived with the two methods are in good agreement, considering their respective uncertainties. The only notable ex-

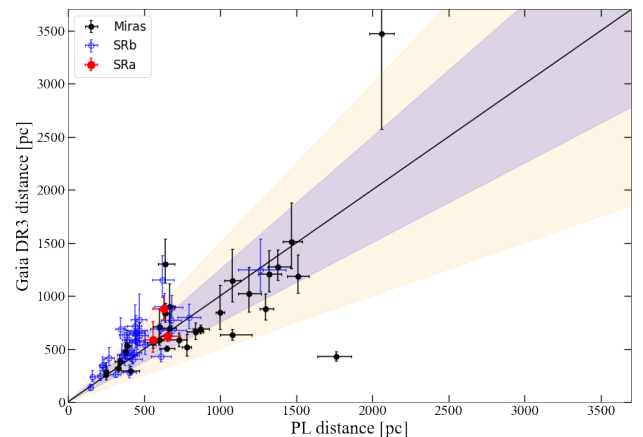


Fig. 10. Comparison between the 'good' *Gaia* DR3 distances (see text) and the PL distances for the same sources. The black line shows the 1-to-1 relation. The blue and orange regions show the range of ± 25 and ± 50 %, respectively.

ception is the carbon star LP And, whose derived PL distance is about 4 times larger than its *Gaia* DR3 distance. The nominal *Gaia* DR3 parallax fractional error of LP And is about 10 %, but the corresponding astrometric excess noise is almost as large as the value of its parallax (~ 99 %). Moreover, LP And is a very faint star, with a magnitude of $G = 17.6$ mag. As we did not apply any correction to the parallax error of such faint stars, the parallax fractional error that we used to calculate the *Gaia* distance of this source could be underestimated. On the other hand, LP And has a period of 614 days, outside the range of periods with which we derived our Mira PL relation, which could have led to this observed discrepancy. The good agreement between the derived *Gaia* DR3 and PL distances for the Miras in Fig. 10, within their respective uncertainties, demonstrates the reliability of our new PL relation based on the VLBI distances for Mira variables. The distances of some of the SRs derived with the PL relation by Knapp et al. (2003) are slightly deviant from the corrected *Gaia* DR3 distances, some differing by ≥ 50 %. There is no clear distinction between the SRas and SRBs. This discrepancy in the two methods is likely due to uncertainties related to the complex pulsation behaviour of these SRs and highlights the need for a better-constrained PL relation for these sources.

Comparison with the NESS catalogue

A new distance catalogue for evolved stars was recently published by Scicluna et al. (2021) as part of the Nearby Evolved Stars Survey (NESS⁶). The NESS catalogue comprises distances for more than 800 stars, including AGB stars as well as other giants and supergiants. Their distances for AGB stars that are beyond ~ 400 pc are based on a new metric derived from the luminosity probability distribution of AGB stars in the LMC. In addition, the NESS catalogue provides distances based on previous maser, *Tycho-Gaia* Astrometric Solution (TGAS) of *Gaia* Data Release 1 (DR1), and *Hipparcos* inverted parallaxes, with parallax fractional errors within 25 %. About 55 % of the sources in the DEATHSTAR sample have distances in the NESS catalogue, mainly based on their new luminosity distance metric

⁶ <https://evolvedstars.space/catalogue/>

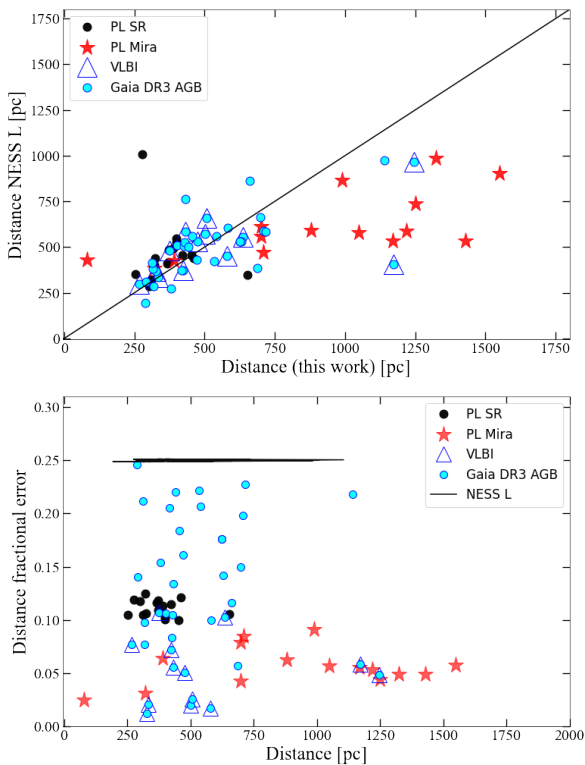


Fig. 11. Comparison with the NESS luminosity distance. **Top:** the NESS luminosity distance (L) compared with the distances calculated with the various methods used in this work. The black line shows the 1-to-1 relation. **Bottom:** The distance fractional errors obtained in this work and those derived with the NESS luminosity distance.

($\sim 37\%$), *Hipparcos* data ($\sim 16\%$), and previous maser measurements ($\sim 2\%$). Figure 11 shows that the NESS luminosity distances agree reasonably well with the distances that were derived in this work, in particular for sources within 750 pc (in our distance). The errors on the NESS luminosity distances are fixed to 25% for all sources, whereas the fractional errors on the distances that we derived change from source to source and are below 25% for all the sources that are in both the NESS and the DEATHSTAR samples.

RUWE

The re-normalised unit weight error or RUWE was introduced by Lindegren (2018) for *Gaia* DR2 and is a measure of the goodness-of-fit of astrometric data. As previously mentioned, the RUWE and the astrometric excess noise both measure discrepancies due to photocentric motions. The astrometric excess noise is expressed as an angle with an ideal value of 0 mas for a good fit, while the RUWE is dimensionless, with an ideal value of 1.0 for well-behaved sources. A value of $\text{RUWE} \leq 1.4$ is the criterion for good astrometric solutions. Lindegren (2018) obtained that 1.4 good-fit criterion by looking at the shape of the distribution of RUWE for a sample of 338 833 sources within 100 pc of the Sun. In their work, the distribution of RUWE follows a normal distribution that peaks at approximately 1.0, but exhibits a long tail towards higher values, with a breakpoint at $\text{RUWE} \approx 1.4$.

The distribution of the RUWE of the sources in the DEATHSTAR sample that have a *Gaia* DR3 distance fractional error within 25% has a shape similar to the distribution in Lindegren (2018), as seen in Fig. 12, with a median value of ~ 1.2 and a tail reaching a maximum RUWE of ~ 4.8 . The RUWE of about 40% of these sources whose derived *Gaia* distances are reliable are smaller than or equal to 1.4. Although the RUWE of the sources with distance fractional errors larger than 25% can reach higher values (~ 8.8), more than 20% of these sources have a RUWE within the 1.4 good-fit criterion. Therefore, a RUWE value of 1.4 does not guarantee reliable distance estimates, and we caution against the use of only the RUWE to assess the quality of astrometric data from *Gaia* DR3 for AGB stars. Figure 12 also shows that, irrespective of the RUWE, bright stars ($G < 8$ mag) are dominant in the sample of sources with distance fractional error larger than 25%. There is no clear trend with the distance fractional error and the colour.

Lindegren (2018) found that the RUWE parameter is most useful to assess the quality and reliability of the astrometric data of samples that include extremely bright, red or blue sources. However, the results of Fabricius et al. (2021) showed that the RUWE value in *Gaia* DR3 for bright sources in crowded areas is strongly underestimated. The RUWE can be used to detect unresolved binaries (Lindegren et al. 2021). Stassun & Torres (2021) found that, due to its high sensitivity to photocenter motions, a RUWE that is even slightly greater than 1.0 may indicate the presence of unresolved binaries. About 78% of the sources in the DEATHSTAR sample have a RUWE higher than 1.0. For AGB stars, however, a high RUWE is more likely caused by saturation of the detector, the large size of the star, and/or the photocentre shift caused by convective motions on the stellar photosphere.

7. Summary and conclusions

A number of studies have shown that the parallaxes of AGB stars measured with *Gaia* are bound to have large errors, as their intrinsic properties bring additional uncertainties to the parallax measurements (circumstellar dust, colour, large size, and surface brightness variability; Chiavassa et al. 2018; Xu et al. 2019; El-Badry et al. 2021). Deriving distances from parallaxes in general is not a straightforward process, and the large errors of the parallaxes of AGB stars make it even more complicated. In this work, we assessed the *Gaia* DR3 parallaxes and the corresponding distances for two samples of nearby AGB stars, the DEATHSTAR and the VLBI samples. Our main results can be summarised as follows.

The standard errors of the *Gaia* DR3 parallaxes are underestimated by more than a factor of 5 for the brightest sources ($G < 8$ mag), based on a comparison with the more robust VLBI parallaxes. Introducing the astrometric excess noise in the total error, as was done for *Gaia* DR2, would overestimate the uncertainties. The excess noise for DR3 is higher than the DR2 excess noise for $\geq 60\%$ of the sources in both samples.

We inferred distances from parallaxes using a Bayesian approach that follows the procedure in Bailer-Jones (2015). This method requires the use of a prior that provides information on the distances. The best prior is one that uses all available information on the sources in order to obtain the most realistic distances. We introduced the AGB prior which follows the Galactic distribution of AGB stars by Jura & Kleinmann (1990), with a scale height of 240 pc and a scale length of 3500 pc. The most important parameter in this inference problem is the fractional error on the measured parallaxes. Our results confirmed the higher limit on the parallax fractional error of 0.2 stated by

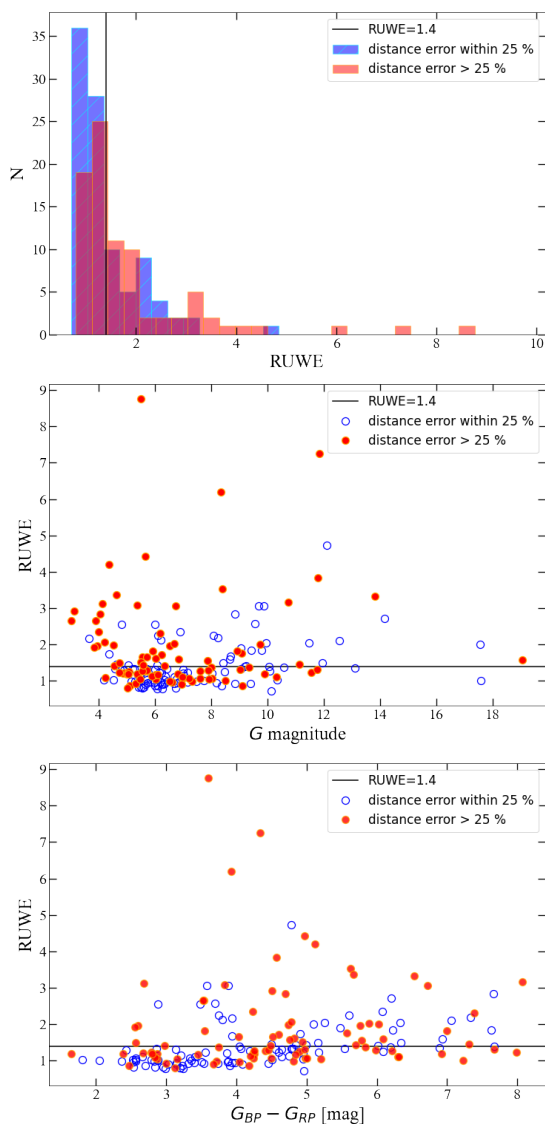


Fig. 12. Assessment of the RUWE criterion. **Top:** Distribution of the RUWE of the sources in the DEATHSTAR sample for the 'good' (blue) and 'bad' (red) derived *Gaia* DR3 distances. **Middle:** RUWE of the sources in the DEATHSTAR sample as a function of *G* magnitude, where the blue open circles and the red full circles represent distances with fractional error within and above 25 %, respectively. **Bottom:** RUWE of the sources in the DEATHSTAR sample as a function of colour. The symbols are the same as above.

Bailer-Jones (2015) for good measurements. Below that limit, the posterior distribution of the distance is closely related to the likelihood of the measurements and to $1/\varpi$. This was the case for the VLBI sample and more than half of the DEATHSTAR sample, using the corrected *Gaia* DR3 parallaxes. For the remaining sources with fractional errors above 0.2, the posterior is dominated by the prior, and the errors on the distances are usually large and asymmetrical. The AGB prior, although representative of the distribution of AGB stars, is highly sensitive to the level of fractional noise, and some cases of non-convergence were observed due to the constraints imposed by the prior. The estimated distances present large uncertainties when the fractional parallax

errors are large, irrespective of the prior used. They are also less likely to be close to the values given by $1/\varpi$. It is important to note that the measured parallax ϖ is not the true parallax, and adopting the distance as the inverse of the measured parallax is not reliable.

The radiative code DUSTY was used to determine the luminosity of the VLBI sources using the better-constrained distances obtained with the VLBI parallaxes. We used the calculated luminosities to derive a new bolometric PL relation for oxygen-rich Mira variables in the Milky Way, valid for periods between 276 and 514 days. We obtained a PL relation of the form $M_{\text{bol}} = (-3.31 \pm 0.24) [\log P - 2.5] + (-4.317 \pm 0.060)$. The PL relation for M-type Mira variables in the Galaxy derived in this work does not significantly differ from existing bolometric PL relations for C-type Miras in the LMC and in the Milky Way (e.g. Feast et al. 2006; Whitelock et al. 2006, 2009).

We provided a new distance catalogue for about 200 nearby AGB stars estimated from VLBI and corrected DR3 *Gaia* parallaxes, and PL relations for Mira (this work) and SR (Knapp et al. 2003) variables. Finally, we caution against the use of the RUWE parameter as the sole measure of the quality of *Gaia* DR3 astrometric data for individual AGB stars, as a RUWE below 1.4 does not guarantee reliable distance estimates.

Acknowledgements. The authors are grateful to Kjell Eriksson for computing the MARCS models, and Sara Bladh for the helpful discussions on the stellar spectra for the SED modelling. We thank the referee for their constructive feedback on the manuscript. EDB acknowledges financial support from the Swedish National Space Agency. WV acknowledges support from the Swedish Research Council through grant No. 2020-04044. This project has received funding from the European Research Council (ERC) under the European Union's Horizon 2020 research and innovation programme under grant agreements No. 883867 [EXWINGS]. This work presents results from the European Space Agency (ESA) space mission *Gaia*. *Gaia* data are being processed by the *Gaia* Data Processing and Analysis Consortium (DPAC). Funding for the DPAC is provided by national institutions, in particular the institutions participating in the *Gaia* MultiLateral Agreement (MLA). The *Gaia* mission website is <https://www.cosmos.esa.int/gaia>. The *Gaia* archive website is <https://archives.esac.esa.int/gaia>. This research made use of Astropy,⁷ a community-developed core Python package for Astronomy (Astropy Collaboration et al. 2013, 2018). This research has made use of the VizieR catalogue access tool and the SIMBAD database, operated at CDS, Strasbourg, France.

References

- Ahmad, A., Freytag, B., & Höfner, S. 2022, A&A, submitted
 Andriantsaralaza, M., Ramstedt, S., Vlemmings, W. H. T., et al. 2021, A&A, 653, A53
 Aringer, B., Marigo, P., Nowotny, W., et al. 2019, MNRAS, 487, 2133
 Astraatmadja, T. L. & Bailer-Jones, C. A. L. 2016a, ApJ, 832, 137
 Astraatmadja, T. L. & Bailer-Jones, C. A. L. 2016b, ApJ, 833, 119
 Astropy Collaboration, Price-Whelan, A. M., Sipőcz, B. M., et al. 2018, AJ, 156, 123
 Astropy Collaboration, Robitaille, T. P., Tollerud, E. J., et al. 2013, A&A, 558, A33
 Bailer-Jones, C. A. L. 2015, PASP, 127, 994
 Bailer-Jones, C. A. L., Rybizki, J., Foesneau, M., Demleitner, M., & Andrae, R. 2021, AJ, 161, 147
 Bailer-Jones, C. A. L., Rybizki, J., Foesneau, M., Mantelet, G., & Andrae, R. 2018, AJ, 156, 58
 Bladh, S., Höfner, S., Nowotny, W., Aringer, B., & Eriksson, K. 2013, A&A, 553, A20
 Carrasco, J. M., Evans, D. W., Montegriffo, P., et al. 2016, A&A, 595, A7
 Chiavassa, A., Freytag, B., & Schultheis, M. 2018, A&A, 617, L1
 Chiavassa, A., Kravchenko, K., Millour, F., et al. 2020, A&A, 640, A23
 Chibueze, J. O., Urago, R., Omodaka, T., et al. 2020, PASJ, 72, 59
 El-Badry, K., Rix, H.-W., & Heintz, T. M. 2021, MNRAS, 506, 2269
 Engels, D., Etoka, S., Gérard, E., & Richards, A. 2015, in Astronomical Society of the Pacific Conference Series, Vol. 497, Why Galaxies Care about AGB Stars III: A Closer Look in Space and Time, ed. F. Kerschbaum, R. F. Wing, & J. Hron, 473

⁷ <http://www.astropy.org>

- Etoka, S., Engels, D., Gérard, E., & Richards, A. M. S. 2018, in *Astrophysical Masers: Unlocking the Mysteries of the Universe*, ed. A. Tarchi, M. J. Reid, & P. Castangia, Vol. 336, 381–384
- Etoka, S. & Le Squeren, A. M. 2000, *A&AS*, 146, 179
- Fabrigius, C., Luri, X., Arenou, F., et al. 2021, *A&A*, 649, A5
- Feast, M. W. & Whitelock, P. A. 2000, *MNRAS*, 317, 460
- Feast, M. W., Whitelock, P. A., & Menzies, J. W. 2006, *MNRAS*, 369, 791
- Freytag, B., Liljegren, S., & Höfner, S. 2017, *A&A*, 600, A137
- Gaia Collaboration, Brown, A. G. A., Vallenari, A., et al. 2018, *A&A*, 616, A1
- Gaia Collaboration, Brown, A. G. A., Vallenari, A., et al. 2021, *A&A*, 649, A1
- Gaia Collaboration, Brown, A. G. A., Vallenari, A., et al. 2016a, *A&A*, 595, A2
- Gaia Collaboration, Prusti, T., de Bruijne, J. H. J., et al. 2016b, *A&A*, 595, A1
- Gaia Collaboration, Vallenari, A., Brown, A. G. A., et al. 2022, *arXiv e-prints*, arXiv:2208.00211
- González Delgado, D., Olofsson, H., Kerschbaum, F., et al. 2003, *A&A*, 411, 123
- Groenewegen, M. A. T. 2021, *A&A*, 654, A20
- Groenewegen, M. A. T., Barlow, M. J., Blommaert, J. A. D. L., et al. 2012, *A&A*, 543, L8
- Groenewegen, M. A. T., de Jong, T., van der Blik, N. S., Slijkhuis, S., & Willems, F. J. 1992, *A&A*, 253, 150
- Gustafsson, B., Edvardsson, B., Eriksson, K., et al. 2008, *A&A*, 486, 951
- Herman, J., Baud, B., Habing, H. J., & Winnberg, A. 1985, *A&A*, 143, 122
- Höfner, S. & Olofsson, H. 2018, *A&A Rev.*, 26, 1
- Ishihara, D., Kaneda, H., Onaka, T., et al. 2011, *A&A*, 534, A79
- Ivezic, Z., Nenkova, M., & Elitzur, M. 1999, *DUSTY: Radiation transport in a dusty environment*
- Jackson, T., Ivezić, Ž., & Knapp, G. R. 2002, *MNRAS*, 337, 749
- Jorissen, A. & Knapp, G. R. 1998, *A&AS*, 129, 363
- Jura, M. & Kleinmann, S. G. 1990, *ApJ*, 364, 663
- Jura, M. & Kleinmann, S. G. 1992, *ApJS*, 79, 105
- Justtanont, K. & Tielens, A. G. G. M. 1992, *ApJ*, 389, 400
- Kamezaki, T., Nakagawa, A., Omodaka, T., et al. 2016a, *PASJ*, 68, 71
- Kamezaki, T., Nakagawa, A., Omodaka, T., et al. 2016b, *PASJ*, 68, 75
- Knapp, G. R., Pourbaix, D., Platais, I., & Jorissen, A. 2003, *A&A*, 403, 993
- Kurayama, T., Sasao, T., & Kobayashi, H. 2005, *ApJ*, 627, L49
- Lewis, B. M. 2002a, in *American Astronomical Society Meeting Abstracts*, Vol. 201, American Astronomical Society Meeting Abstracts, 25.06
- Lewis, B. M. 2002b, *ApJ*, 576, 445
- Lian, J., Zhu, Q., Kong, X., & He, J. 2014, *A&A*, 564, A84
- Lindgren, L. 2018, in *Gaia Data Processing and Analysis Consortium*
- Lindgren, L., Klioner, S. A., Hernández, J., et al. 2021, *A&A*, 649, A2
- Lindgren, L., Lammers, U., Hobbs, D., et al. 2012, *A&A*, 538, A78
- Luri, X., Brown, A. G. A., Sarro, L. M., et al. 2018, *A&A*, 616, A9
- Lutz, T. E. & Kelker, D. H. 1973, *PASP*, 85, 573
- Maercker, M., Brunner, M., Mecina, M., & De Beck, E. 2018, *A&A*, 611, A102
- Matsuura, M., Zijlstra, A. A., Bernard-Salas, J., et al. 2007, *MNRAS*, 382, 1889
- Nakagawa, A., Omodaka, T., Handa, T., et al. 2014, *PASJ*, 66, 101
- Nyu, D., Nakagawa, A., Matsui, M., et al. 2011, *PASJ*, 63, 63
- Olofsson, H., González Delgado, D., Kerschbaum, F., & Schöier, F. L. 2002, *A&A*, 391, 1053
- Ramstedt, S., Schöier, F. L., & Olofsson, H. 2009, *A&A*, 499, 515
- Ramstedt, S., Schöier, F. L., Olofsson, H., & Lundgren, A. A. 2006, *A&A*, 454, L103
- Ramstedt, S., Schöier, F. L., Olofsson, H., & Lundgren, A. A. 2008, *A&A*, 487, 645
- Ramstedt, S., Vlemmings, W. H. T., Doan, L., et al. 2020, *A&A*, 640, A133
- Reid, M. J. & Honma, M. 2014, *ARA&A*, 52, 339
- Ren, F., Chen, X., Zhang, H., et al. 2021, *ApJ*, 911, L20
- Rouleau, F. & Martin, P. G. 1991, *ApJ*, 377, 526
- Samus', N. N., Kazarovets, E. V., Durlevich, O. V., Kireeva, N. N., & Pastukhova, E. N. 2017, *Astronomy Reports*, 61, 80
- Sánchez Contreras, C., Alcolea, J., Rodríguez Cardoso, R., et al. 2022, *arXiv e-prints*, arXiv:2206.12185
- Schlegel, D. J., Finkbeiner, D. P., & Davis, M. 1998, *ApJ*, 500, 525
- Schöier, F. L. & Olofsson, H. 2001, *A&A*, 368, 969
- Scicluna, P., Kemper, F., McDonald, I., et al. 2021, *arXiv e-prints*, arXiv:2110.12562
- Soszyński, I., Wood, P. R., & Udalski, A. 2013, *ApJ*, 779, 167
- Stassun, K. G. & Torres, G. 2021, *ApJ*, 907, L33
- Stephenson, C. B. 1984, *A general catalogue of galactic S stars*, 2nd edn., Publications of the Warner and Swasey Observatory ; v. 3, no. 1 (Cleveland, Ohio: Case Western Reserve University)
- Sun, Y., Zhang, B., Reid, M. J., et al. 2022, *ApJ*, 931, 74
- Trabucchi, M., Mowlavi, N., & Lebzelter, T. 2021, *A&A*, 656, A66
- Urago, R., Yamaguchi, R., Omodaka, T., et al. 2020, *PASJ*, 72, 57
- van Langevelde, H., Quiroga-Núñez, L. H., Vlemmings, W. H. T., et al. 2018, in *14th European VLBI Network Symposium & Users Meeting (EVN 2018)*, 43
- van Langevelde, H. J., van der Heiden, R., & van Schooneveld, C. 1990, *A&A*, 239, 193
- van Leeuwen, F., Evans, D. W., De Angeli, F., et al. 2017, *A&A*, 599, A32
- VERA Collaboration, Hirota, T., Nagayama, T., et al. 2020, *PASJ*, 72, 50
- Vlemmings, W. H. T. & van Langevelde, H. J. 2007, *A&A*, 472, 547
- Vlemmings, W. H. T., van Langevelde, H. J., & Diamond, P. J. 2002, *A&A*, 393, L33
- Vlemmings, W. H. T., van Langevelde, H. J., Diamond, P. J., Habing, H. J., & Schilizzi, R. T. 2003, *A&A*, 407, 213
- Watson, C., Henden, A. A., & Price, A. 2021, *VizieR Online Data Catalog, B/vsx*
- Whitelock, P., Feast, M., & Catchpole, R. 1991, *MNRAS*, 248, 276
- Whitelock, P. A., Feast, M. W., Marang, F., & Groenewegen, M. A. T. 2006, *MNRAS*, 369, 751
- Whitelock, P. A., Feast, M. W., & Van Leeuwen, F. 2008, *MNRAS*, 386, 313
- Whitelock, P. A., Menzies, J. W., Feast, M. W., et al. 2009, *MNRAS*, 394, 795
- Xu, S., Zhang, B., Reid, M. J., Zheng, X., & Wang, G. 2019, *ApJ*, 875, 114
- Yeşilyaprak, C. & Aslan, Z. 2004, *MNRAS*, 355, 601
- Zhang, B., Zheng, X., Reid, M. J., et al. 2017, *ApJ*, 849, 99

Appendix A: Gaia DR3 distances

Table A.1. Derived Gaia DR3 distances.

Source	Parallax frac error*	$r_{\text{AGB}}^{\text{median}}$ [pc]	$\sigma_{r,\text{AGB}}^-$ [pc]	$\sigma_{r,\text{AGB}}^+$ [pc]	$r_{\text{EDSD}}^{\text{median}}$ [pc]	$\sigma_{r,\text{EDSD}}^-$ [pc]	$\sigma_{r,\text{EDSD}}^+$ [pc]
AA Cam	0.13	489	60	79	480	75	57
AA Cyg	0.27	1423	599	1570	747	243	156
AD Cyg	0.2	1520	317	558	1202	243	179
AH Dra	0.21	371	76	130	358	112	69
AI Vol	0.1	583	56	70	573	67	53
AM Cen	0.12	897	103	134	854	113	91
AP Lyn	0.15	495	72	101	480	90	66
AQ And	0.1	768	72	89	756	84	69
BD+06 319	0.18	312	52	80	310	76	52
BK Vir	0.17	242	39	59	242	58	39
BL Ori	0.33	1931	970	1570	751	291	181
BM Gem	0.18	1243	201	293	1129	213	158
BW Cam	0.26	1104	274	505	893	251	169
BX Cam	0.14	554	75	104	537	92	69
BX Eri	0.14	439	58	79	433	75	56
CL Mon	0.27	1563	471	989	1042	281	194
CS Dra	0.16	457	69	99	450	92	66
CSS2 41	0.53	3792	700	497	2398	501	388
CW Cnc	0.11	262	27	35	261	34	27
CZ Hya	0.2	1514	253	364	1366	266	198
DK Vul	0.27	1625	596	1345	926	269	181
DR Ser	0.18	1200	223	369	1010	194	144
DY Gem	0.25	1217	357	838	862	241	163
EP Aqr	0.34	500	299	700	305	369	145
EP Vul	0.3	2124	996	1522	871	281	185
FU Mon	0.13	795	99	132	755	112	86
FV Boo	0.21	885	155	227	857	204	144
GI Lup	0.17	1019	169	254	917	175	129
GX Mon	0.23	727	203	522	570	179	114
GY Aql	0.59	1965	952	1322	731	396	239
HS UMa	0.17	332	52	74	332	75	52
HU Pup	0.44	3390	895	758	1806	435	324
HV Cas	0.14	1205	163	225	1112	171	133
IK Tau	0.19	289	54	88	281	79	50
IRAS 15194-5115	0.14	696	93	129	656	104	79
IRC -10401	0.64	3383	1166	798	1121	414	280
IRC+10365	0.16	519	82	122	488	96	70
IRC+60041	0.14	1300	175	241	1179	172	136
IRC-30398	0.54	2172	1018	1340	812	383	237
L2 Pup	0.25	1043	942	1579	98	190	37
LP And	0.1	428	40	50	423	48	39
NP Pup	0.13	586	70	91	570	83	64
NSV 17351	1.66	3873	687	447	2402	547	424
NSV 24833	0.24	1155	277	513	928	244	167
OH 56.1 +2.1	0.65	3953	616	392	2601	528	414

* corrected parallax fractional error

 $r_{\text{prior}}^{\text{median}}$ the median distance derived with the AGB or EDSD prior. $\sigma_{r,\text{prior}}^{-/+}$ the lower/upper uncertainties of the distance with the AGB or EDSD prior.

Table A.1. continued.

Source	Parallax frac error	$r_{\text{AGB}}^{\text{median}}$ [pc]	$\sigma_{r,\text{AGB}}^-$ [pc]	$\sigma_{r,\text{AGB}}^+$ [pc]	$r_{\text{EDSD}}^{\text{median}}$ [pc]	$\sigma_{r,\text{EDSD}}^-$ [pc]	$\sigma_{r,\text{EDSD}}^+$ [pc]
OZ Gem	0.71	1913	568	866	1339	437	307
PQ Cep	0.08	631	45	54	625	51	45
QX Pup	5.37	3820	706	481	2392	559	433
R And	0.32	655	253	627	478	258	137
R Aql	0.2	308	77	268	266	85	52
R Aqr	0.68	631	263	448	618	434	255
R Cas	0.19	207	41	74	198	60	37
R Cnc	0.24	347	97	235	311	141	75
R Crt	0.17	237	40	64	234	59	39
R Cyg	0.09	555	45	54	548	52	43
R For	0.05	507	24	27	507	27	24
R Gem	0.19	847	159	256	763	174	123
R Hor	0.19	260	48	77	258	75	47
R Hya	0.37	595	350	730	355	386	169
R LMi	0.22	339	73	127	333	118	70
R Lep	0.14	471	64	88	462	82	60
R Lyn	0.13	880	105	138	852	123	97
R Peg	0.24	450	104	186	430	156	93
R Scl	0.16	408	61	86	409	87	61
R UMa	0.26	638	145	245	608	207	130
R Vol	0.11	662	68	86	649	81	65
RR Aql	0.15	513	73	102	492	88	65
RS And	0.25	562	175	491	443	176	102
RS CrA	0.07	1467	97	112	1437	105	91
RT Cap	0.13	564	69	92	551	84	65
RT Sco	0.31	2592	1453	1370	724	271	169
RT Vir	0.29	343	107	233	338	220	104
RV Aqr	0.09	586	50	61	580	59	49
RV Cam	0.22	490	129	324	413	139	85
RV Cyg	0.3	1124	426	1051	698	261	162
RW LMi	0.08	319	22	27	319	27	23
RW Lep	0.16	419	63	91	407	81	58
RX Boo	0.19	181	35	59	180	59	35
RX Lac	0.28	596	228	724	421	204	110
RY Dra	0.1	401	38	47	400	46	38
RY Mon	0.11	875	96	124	835	106	85
RZ Peg	0.11	1275	128	161	1225	141	115
RZ Sgr	0.12	432	50	66	426	62	49
S Aur	0.2	1244	267	494	1000	217	156
S Cas	0.2	965	195	331	833	194	136
S Cep	0.18	534	93	144	504	117	80
S CrB	0.23	443	98	167	433	153	93
S Crt	0.25	548	123	211	530	187	114
S Dra	0.36	707	231	448	603	298	170
S Lyr	1.34	3473	899	706	1770	496	367
S Pav	0.57	1154	626	971	533	458	267
S Sct	0.12	438	50	65	425	59	46
S Ser	0.38	1079	262	414	998	339	225

Table A.1. continued.

Source	Parallax frac error	$r_{\text{AGB}}^{\text{median}}$ [pc]	$\sigma_{r,\text{AGB}}^-$ [pc]	$\sigma_{r,\text{AGB}}^+$ [pc]	$r_{\text{EDSD}}^{\text{median}}$ [pc]	$\sigma_{r,\text{EDSD}}^-$ [pc]	$\sigma_{r,\text{EDSD}}^+$ [pc]
SS Vir	0.22	583	112	173	576	167	108
ST Cam	0.15	625	91	129	597	109	81
ST Her	0.18	324	57	86	319	82	54
ST Sco	0.22	786	197	438	637	178	118
ST Sgr	0.19	608	127	237	534	136	91
SU Vel	0.16	417	68	103	396	85	59
SV Aqr	0.16	445	65	90	443	89	64
SV Peg	0.35	1000	504	1179	501	286	152
SW Vir	0.43	491	245	487	433	411	205
SY Aql	0.2	973	203	358	824	191	135
SY Scl	0.48	1157	261	382	1164	387	264
SZ Car	0.07	689	45	52	681	50	44
SZ Dra	0.13	470	57	75	460	70	54
T Ari	0.42	689	270	533	554	342	185
T Cam	0.21	623	136	248	554	155	102
T Cep	0.34	1315	889	1451	338	322	136
T Cet	0.44	465	193	377	473	388	199
T Dra	0.18	901	146	214	849	175	126
T Ind	0.23	671	139	227	634	188	122
T Lep	0.18	356	61	94	347	85	57
T Lyr	0.08	427	33	38	423	38	31
T Mic	0.25	272	84	240	241	131	63
T Sgr	0.96	2839	1015	1051	1251	448	310
TT Cen	0.13	1182	152	208	1083	154	121
TT Cyg	0.07	671	43	49	664	47	42
TT Tau	0.09	671	59	73	659	68	56
TU Gem	0.38	2129	884	1350	989	340	224
TV Dra	0.18	541	90	134	523	119	83
TW Hor	0.17	481	75	109	475	104	73
TW Oph	0.25	966	356	1276	613	205	128
TW Peg	0.17	278	48	77	269	68	44
TX Cam	0.13	292	35	47	287	44	33
TX Psc	0.28	339	101	223	327	193	94
TY Dra	0.14	699	89	120	681	110	83
TZ Aql	0.13	524	64	84	511	78	60
U Ant	0.14	294	40	54	288	50	38
U Cam	0.13	630	77	102	606	89	70
U Cyg	0.06	687	37	41	681	41	35
U Her	0.17	453	73	110	442	99	69
U Lyn	0.19	925	161	243	855	185	133
U Men	0.09	317	28	34	315	33	27
UU Aur	0.43	1295	642	1212	609	344	194
UX And	0.35	1168	471	1027	700	301	181
UX Cyg	0.29	1682	527	1031	1081	304	209
UX Dra	0.23	567	135	254	510	168	105
UY Cen	0.18	718	127	200	660	145	103
UY Cet	0.22	455	90	143	454	142	89
V Aql	0.26	1045	535	2005	488	193	113

Table A.1. continued.

Source	Parallax frac error	$r_{\text{AGB}}^{\text{median}}$ [pc]	$\sigma_{r,\text{AGB}}^-$ [pc]	$\sigma_{r,\text{AGB}}^+$ [pc]	$r_{\text{EDSD}}^{\text{median}}$ [pc]	$\sigma_{r,\text{EDSD}}^-$ [pc]	$\sigma_{r,\text{EDSD}}^+$ [pc]
V CrB	0.11	836	81	99	829	97	79
V Cyg	0.2	623	136	266	538	141	94
V Hya	0.25	529	131	248	484	177	107
V Tel	0.22	501	117	224	451	145	91
V1302 Cen	0.11	892	91	114	856	100	81
V1426 Cyg	0.16	709	113	168	657	128	92
V1942 Sgr	0.13	650	84	115	622	97	75
V1943 Sgr	0.38	929	561	1062	394	366	170
V1968 Cyg	0.46	2669	1042	1163	1135	380	258
V365 Cas	0.2	1010	206	355	858	194	137
V384 Per	2.64	2712	1087	1123	991	463	310
V386 Cep	0.22	2561	558	849	1820	337	257
V460 Cyg	0.37	1376	649	1300	661	310	182
V466 Per	0.13	685	84	112	655	96	75
V637 Per	0.26	1227	307	568	969	265	181
V644 SCo	0.21	1608	382	779	1179	246	180
V821 Her	0.36	1846	916	1487	731	309	189
V837 Her	0.8	3225	988	858	1499	456	326
V996 Cen	0.11	578	59	74	563	67	55
VX And	0.08	619	49	59	612	56	48
VX Aql	0.25	2394	673	1092	1479	318	234
VY UMa	0.17	444	71	104	437	99	68
W Aql	0.13	380	49	68	369	60	46
W CMa	0.18	777	148	246	681	150	106
W Leo	0.28	961	195	294	943	278	187
W Ori	0.41	926	391	800	602	333	187
W Pic	0.08	594	43	49	590	48	42
WY Cas	0.17	1141	196	302	1001	190	141
WZ Cas	0.07	465	33	38	460	37	32
X Cnc	0.36	754	238	455	641	298	174
X Her	0.17	137	23	34	136	34	22
X Hya	0.23	482	115	221	441	153	93
X TrA	0.28	941	505	1683	430	210	114
X Vel	0.11	631	65	82	615	75	61
XZ Vel	0.15	1151	162	228	1049	165	128
Y CVn	0.29	397	110	213	397	214	110
Y Hya	0.23	551	130	248	495	163	101
Y Lib	0.22	1055	196	294	985	237	167
Y Lyn	0.21	422	92	168	396	128	79
Y Pav	0.41	980	307	548	797	336	209
Y Scl	0.3	406	120	244	398	229	115
Y Tau	0.2	782	169	318	669	168	115
Y Tel	0.18	442	77	118	426	103	70
Y UMa	0.17	348	57	83	346	83	56
Z Ant	0.28	1106	291	540	883	269	178
Z Psc	0.18	660	107	157	638	140	99
θ Aps	0.23	203	75	886	157	88	40
χ Cyg	0.24	1272	1058	2327	209	115	55

Appendix B: SED fitting with DUSTY

The spectral energy distributions (SEDs) of the sources in the VLBI and DEATHSTAR samples were modelled using the radiative transfer code DUSTY (Ivezic et al. 1999). A central star is surrounded by a dusty shell following a r^{-2} -density law, and with an outer to inner radius fraction of 10^4 . All dust grains were assumed to have a radius $a = 0.1 \mu\text{m}$. The modelled VLBI sources are M-type stars for which the grains were assumed to be silicate-type with the optical properties from Justtanont & Tielens (1992). We used the high-resolution MARCS⁸ model atmospheres (Gustafsson et al. 2008, private communication) as input stellar spectra for the M-type stars. The corresponding stellar temperature ranges from 2400 to 3600 K. The chosen models have a surface gravity, $\log g$, of -0.5 , which is within the range of the values of $\log g$ obtained from the 3D hydrodynamical models of AGB stars of Freytag et al. (2017) and Ahmad et al. (2022); and a microturbulence of 0.5 km s^{-1} as in Olofsson et al. (2002). The resolution of the MARCS spectra was reduced by convolving them with a Gaussian kernel with a standard deviation of 250. The diluted spectra were then re-gridded. As the MARCS spectra end at $20 \mu\text{m}$, they were extrapolated to longer wavelengths, up to 3.6 cm , with a Rayleigh-Jeans tail.

For the carbon stars, the dust grains were assumed to be amorphous carbons with optical properties derived by Rouleau & Martin (1991). We used the COMARCS⁹ model atmospheres (Aringer et al. 2019) for the stellar spectra of the carbon stars, with temperatures between 2500 and 3300 K, and the same $\log g$ and microturbulence as the MARCS models. The type of dust and input stellar spectra of the S-type stars were either similar to the C- or the M-type stars, depending on their spectral class or colour, as in Ramstedt et al. (2006). A large grid of radiative transfer models with varying temperature, with steps of 100 K ($T_\star = 2400 - 3600 \text{ K}$ and $2500 - 3300 \text{ K}$ for the oxygen- and carbon-rich models, respectively); dust temperature at the inner radius of the dust shell, T_d , ranging from 600 to 1200 K for the oxygen-rich models, and up to 1300 K for the carbon-rich models, with steps of 100 K; and dust optical depth at $10 \mu\text{m}$ ($\tau_{10} = 0.01 - 5.00$, with steps of 0.01) was constructed. We made use of the scaling properties of the dust radiative transfer in a spherically symmetric envelope to determine either the luminosity, knowing the distance, or the other way around. We used the former to derive a new PL relation with the VLBI sources using their distances obtained from maser parallaxes (Sect. 5). The latter was used to determine the distances of the sources whose *Gaia* DR3 distances are not reliable or for direct comparison with the *Gaia* distances (Sect. 6).

For each star, the DUSTY input parameters, which are T_\star , T_d , and τ_{10} , and the bolometric stellar luminosity, L_\star , or the distance, r , were constrained by photometric flux densities collected from various online catalogues. The data consist of G , G_{BP} , and G_{RP} fluxes from *Gaia* DR3; J -, H -, and K_s -band fluxes from 2MASS (quality flag rd_flg between 1 and 3); 3.5 and $4.9 \mu\text{m}$ fluxes (L and M bands, respectively) from DIRBE; 12 , 25 , 60 , $100 \mu\text{m}$ fluxes from the *IRAS* point source catalogue (quality flag 3), and fluxes at 8.6 up to $160 \mu\text{m}$ from Akari (quality flag 3) collected from the ViZier photometry viewer¹⁰ online tool. We did not include WISE data as AGB stars are known to saturate the WISE photometric instruments, in particular in the $W1$ and $W2$ bands, requiring additional calibrations to correct

for residual biases (Lian et al. 2014). The fluxes were corrected for interstellar extinction using the visual extinction coefficient, A_V , given by Eq.(8) in Groenewegen et al. (1992). The A_λ/A_V ratios were taken from Schlegel et al. (1998) and interpolated for the relevant wavelengths. Extinction beyond $3.5 \mu\text{m}$ was neglected.

Ramstedt et al. (2008) assessed the effect of variability on the flux using several measurements from different epochs. Their results show that the variability of the star, which is particularly important at short wavelengths, can be accounted for in the uncertainty assumed for each flux point. Uncertainties of 60 %, 50 %, and 40 % were assigned to fluxes in the J , H , and K bands, respectively. For the L and M bands, a flux uncertainty of 30 % was assumed. The properties of variability at longer wavelengths are less clear due to scarce data. A 20 % calibration uncertainty was assigned to flux points beyond $5 \mu\text{m}$. The *Gaia* bands were not covered in Ramstedt et al. (2008). As the amplitude of the variation is the largest at short wavelengths, we assumed an uncertainty of 75% for the fluxes measured at the three *Gaia* bands.

The model grid SEDs were scaled according to the median distance, r_{median} , derived using the VLBI parallax and the AGB prior (or the luminosity derived with our new PL relation) until a satisfactory fit to the observational data was obtained. The best-fit to the DUSTY input parameters (see Fig. B.1) was found using the same χ^2 -minimization strategy as in Ramstedt et al. (2009), for example. Thereby, T_\star , T_d , τ_{10} , and L_\star (or r) were estimated for each source. As the derived VLBI distance (or the luminosity calculated using the PL relation derived in Sect. 5) follows a distribution centred on r_{median} (L_\star^{median}) with known lower and upper limits, we checked whether the best fit model significantly changed for the extreme distances (luminosities). We then optimised the flux scaling with the now-known T_\star , T_d , and τ_{10} parameters. We created a posterior distribution on the luminosity L_\star (distance r) by applying the weighted bootstrap statistical method which consists of randomly selecting a distance (luminosity) from the weighted distance (luminosity) distribution and fitting it to a sub-sample of the observed photometric data selected at random. This process was repeated 4 000 times, which allowed us to derive a median luminosity, L_\star^{median} (distance, r_{median}), along with the 16 and 84 percentiles of the generated luminosity (distance) distribution as its confidence interval. The derived parameters are listed in Tables 3 and B.1.

The SEDs of a number of the sources that we modelled were poorly fitted. This is particularly obvious for HU Pup, QX Pup, and UX Cyg in the VLBI sample. The poor fit of QX Pup could be explained by its complex transition nature. As previously mentioned, QX Pup is classified as an OH/IR star. It is the central star of the bipolar nebula OH231.8, and is part of a system with a binary companion and a rotating circumbinary disk (Sánchez Contreras et al. 2022). The poor fit of UX Cyg could be due to its unusually turbulent envelope (Etoka et al. 2018). There is no record of signs of irregularities for the SRA variable HU Pup in the literature. For sources such as S Ser and NSV 17351, the data points were not properly fitted in the long wavelength part of the SED. In fact, the SED of a few sources exhibit a second bump at longer wavelengths (e.g. NSV 17351, GI Lup, RT Sco, TT Cen), which is usually observed in sources with a detached shell. For such sources, the SED is usually fitted with two black bodies, which was not attempted in this paper.

⁸ //marcs.astro.uu.se/

⁹ http://stev.oapd.inaf.it/atm/lrspe.html

¹⁰ http://vizier.unistra.fr/vizier/sed/

Comparison between black body and model atmosphere

We compared the results of the SED fitting when using a black body as stellar radiation input with the results obtained with model atmospheres. We found that the results between the two methods differ the most for oxygen-rich stars due to the strong TiO absorption in their spectra at short wavelengths. Overall, the luminosity is lower by about 25 % with the MARCS models compared to with a black body. When using model atmospheres, the dust condensation temperature is systematically lower than what one obtains with a black body, by up to 35 %, while the corresponding effective temperatures tend to be higher, by up to 30 %, for oxygen-rich stars. The optical depths at $10 \mu\text{m}$ obtained with the two methods are in good agreement in the low- τ_{10} regime ($\tau_{10} < 0.8$). Above that, the optical depths derived using model atmospheres tend to be smaller.

Table B.1. DUSTY results for the Miras in the DEATHSTAR sample for which distances were derived using our new PL relation.

Source	P [days]	dust*	T_{\star} [K]	T_{dust} [K]	τ_{10}	$L_{\star}^{\text{median}}$ [L_{\odot}]	$\sigma_{L_{\star}}^{-}$ [L_{\odot}]	$\sigma_{L_{\star}}^{+}$ [L_{\odot}]	$r_{\text{PL(M)}}$ [pc]	$\sigma_{r,\text{PL(M)}}^{-}$ [pc]	$\sigma_{r,\text{PL(M)}}^{+}$ [pc]
<i>C-type</i>											
AFGL 3068	696	AMC	2500	800	1.2	11890	1013	1108	1220	60	70
AI Vol	511	AMC	2500	1300	0.28	7897	525	563	730	60	50
CL Mon	493	AMC	3100	1300	0.05	7532	485	518	910	30	40
CZ Hya	442	AMC	2500	1200	0.09	6518	376	399	1470	60	70
HV Cas	527	AMC	3100	1300	0.09	8226	563	604	1320	70	80
IRAS 15194-5115	576	AMC	3000	1200	0.36	9254	683	738	670	40	40
IRC+10216	630	AMC	3100	1300	0.5	10420	826	897	190	20	20
IRC+60041	280	AMC	2500	1300	0.07	3561	104	107	640	50	60
LP And	614	AMC	2500	1300	3	10071	783	849	1760	120	100
PQ Cep	442	AMC	2500	1300	0.04	6517	376	399	1080	80	130
R For	386	AMC	2500	1300	0.06	5447	268	282	650	50	50
R Lep	445	AMC	3300	1100	0.02	6576	382	405	380	20	10
R Vol	453	AMC	2500	1300	0.13	5076	233	244	840	60	50
RV Aqr	453	AMC	3100	1300	0.1	6733	398	423	600	30	30
RZ Peg	437	AMC	2700	900	0.01	6420	365	388	1380	70	80
S Cep	484	AMC	3100	1300	0.03	7350	465	496	390	20	20
T Dra	422	AMC	2500	1300	0.07	6134	337	356	670	50	30
U Cyg	463	AMC	3000	800	0.02	6930	419	446	870	50	60
V CrB	358	AMC	3100	1300	0.02	4930	220	230	640	20	30
V Cyg	421	AMC	2500	1200	0.07	6116	335	354	420	10	20
V358 Lup	632	AMC	2500	1300	0.75	10464	831	903	1050	60	60
V384 Per	535	AMC	3100	1200	0.12	8393	582	626	700	30	30
V688 Mon	1770	AMC	2900	1000	0.34	40914	5699	6622	3370	250	260
V821 Her	524	AMC	2500	1300	0.2	8165	556	597	700	61	50
V1259 Ori	696	AMC	2500	1300	0.75	11890	1013	1108	1550	90	90
V1426 Cyg	470	AMC	2500	1300	0.07	7070	435	463	600	40	20
V1968 Cyg	395	AMC	2600	1300	0.55	5625	286	301	990	80	100
<i>S-type</i>											
GI Lup	469	AMC	2600	900	0.01	7050	432	461	1190	70	80
IRC-10401	480	AMS	2600	600	5	7270	456	487	3470	120	110
NSV 24833	418	AMS	2400	900	4	6053	328	347	3500	120	140
R And	409	AMS	3400	600	0.06	5885	312	329	390	30	20
R Cyg	427	AMS	2600	600	0.03	6226	346	366	560	40	30
R Gem	370	AMC	3200	1300	0.03	5151	241	252	1000	30	30
R Lyn	366	AMC	3200	1300	0.03	5076	233	244	1300	40	50
RT Sco	449	AMS	2600	1200	0.3	6655	391	415	710	60	60
S Cas	608	AMS	3000	1000	0.7	9946	767	831	880	60	50

P : period in days.

* dust type taken from Ramstedt et al. (2006)

AMC: amorphous carbon.

AMS: amorphous silicate.

T_{\star} is the stellar temperature; T_{dust} the dust temperature; τ_{10} the optical depth at $10 \mu\text{m}$.

$L_{\star}^{\text{median}}$ the median luminosity; $\sigma_{L_{\star}}^{-/+}$ the lower/upper uncertainties on the luminosity.

$r_{\text{PL(M)}}$ the median distance calculated with our new PL relation;

$\sigma_{r,\text{PL(M)}}^{-/+}$ the lower/upper uncertainties on the PL distance.

Table B.1. continued.

Source	P [days]	dust*	T_{\star} [K]	T_{dust} [K]	τ_{10}	$L_{\star}^{\text{median}}$ [L_{\odot}]	$\sigma_{L_{\star}}^{-}$ [L_{\odot}]	$\sigma_{L_{\star}}^{+}$ [L_{\odot}]	$r_{\text{PL(M)}}$ [pc]	$\sigma_{r_{\text{PL(M)}}}^{-}$ [pc]	$\sigma_{r_{\text{PL(M)}}}^{+}$ [pc]
S Lyr	438	AMS	3100	600	0.44	6447	369	391	2060	80	80
ST Sgr	400	AMS	2600	600	0.03	5711	294	310	720	40	70
T Cam	369	AMC	2500	1300	0.04	5138	239	251	980	30	40
T Sgr	396	AMC	2700	1000	0.02	5635	287	302	1010	50	50
TT Cen	462	AMS	3000	1200	0.11	6910	417	444	1510	70	70
VX Aql	643	AMC	2700	700	0.01	10706	862	937	2450	110	120
W And	397	AMS	2600	600	0.02	5660	289	305	350	20	20
W Aql	479	AMS	2700	1200	0.7	7249	454	484	340	31	30
WY Cas	482	AMS	2700	600	0.12	7300	460	490	1080	50	50
χ Cyg	408	AMS	2600	1200	0.17	5862	309	326	180	10	5
<i>M-type</i>											
BW Cam	628	AMS	3000	800	0.8	10376	820	891	1250	50	60
GX Mon	527	AMS	3500	800	5	8227	563	605	1430	70	70
GY Aql	464	AMS	2900	1200	0.3	6950	421	449	410	40	40
IK Tau	470	AMS	3000	900	0.8	7070	435	463	250	10	10
IRC-10529	675	AMS	3600	1200	4	11417	952	1039	930	70	60
IRC-30398	575	AMS	3100	1200	1.4	9233	681	735	670	50	40
IRC+10365	455	AMS	3000	600	0.7	6773	403	428	780	30	30
IRC+40004	720	AMS	2400	1200	2.5	12435	1085	1189	1160	60	70
KU And	720	AMS	2400	1200	2.5	12435	1085	1189	1170	70	60
NV Aur	635	AMS	3500	1100	4	10530	840	912	1325	65	65
R Cas	430	AMS	2900	1200	0.28	6293	353	374			
R Hor	408	AMS	3100	600	0.04	5862	309	326	250	10	10
R Leo	312	AMS	2900	1200	0.11	4113	148	154	100	5	5
R LMi	372	AMS	2900	1200	0.19	5191	244	256	320	10	10
T Ari	314	AMS	3100	700	0.01	4145	151	157	290	5	10
T Cep	388	AMS	2900	800	0.02	5487	273	287	150	2	2
TX Cam	559	AMS	3000	1200	0.7	8894	640	690	410	60	60
U Men	409	AMS	2900	600	0.04	5881	311	328	330	20	10
WX Psc	660	AMS	3400	1100	4	11082	909	991	720	30	30

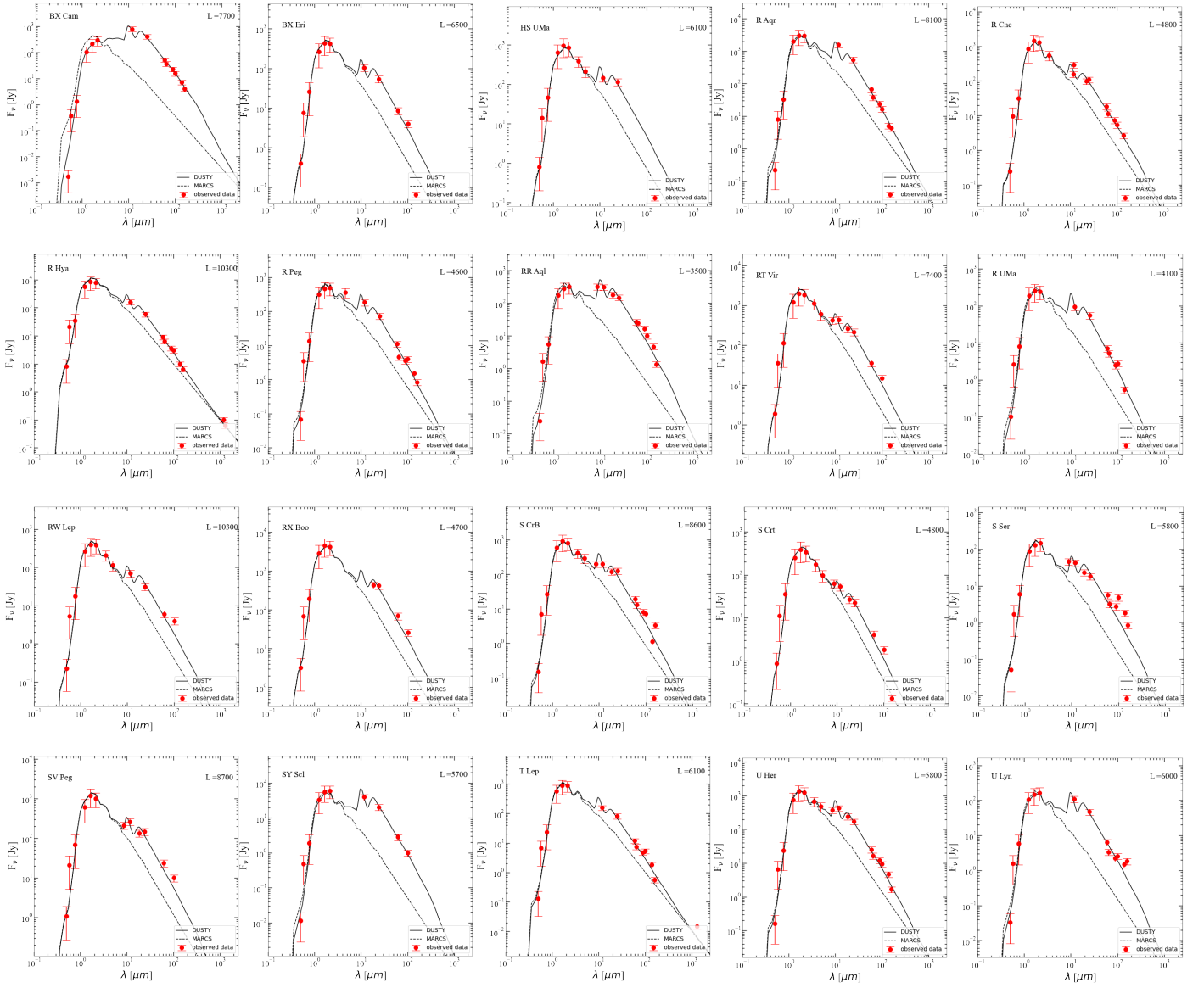


Fig. B.1. SED fitting of the stellar and dust emission with DUSTY for the sources in the VLBI sample. The name of each source is given in the upper left corner of each panel, and the derived luminosity is given in the upper right corner, in solar luminosity.

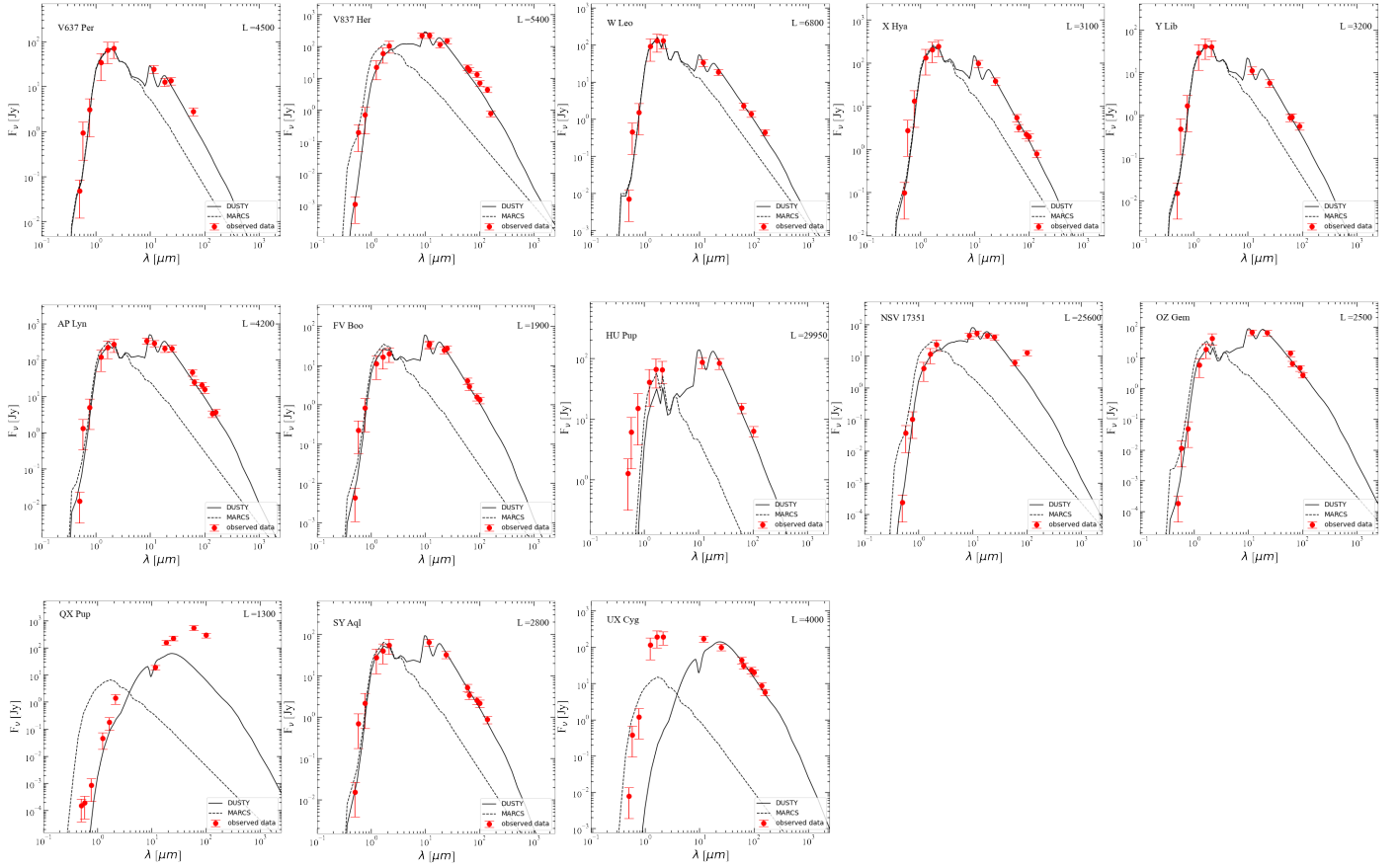


Fig. B.2. SED fitting of the stellar and dust emission with DUSTY for the sources in the VLBI sample. The name of each source is given in the upper left corner of each panel, and the derived luminosity is given in the upper right corner, in solar luminosity. The last two rows correspond to the outliers that were excluded from the PL relation determination (see text).

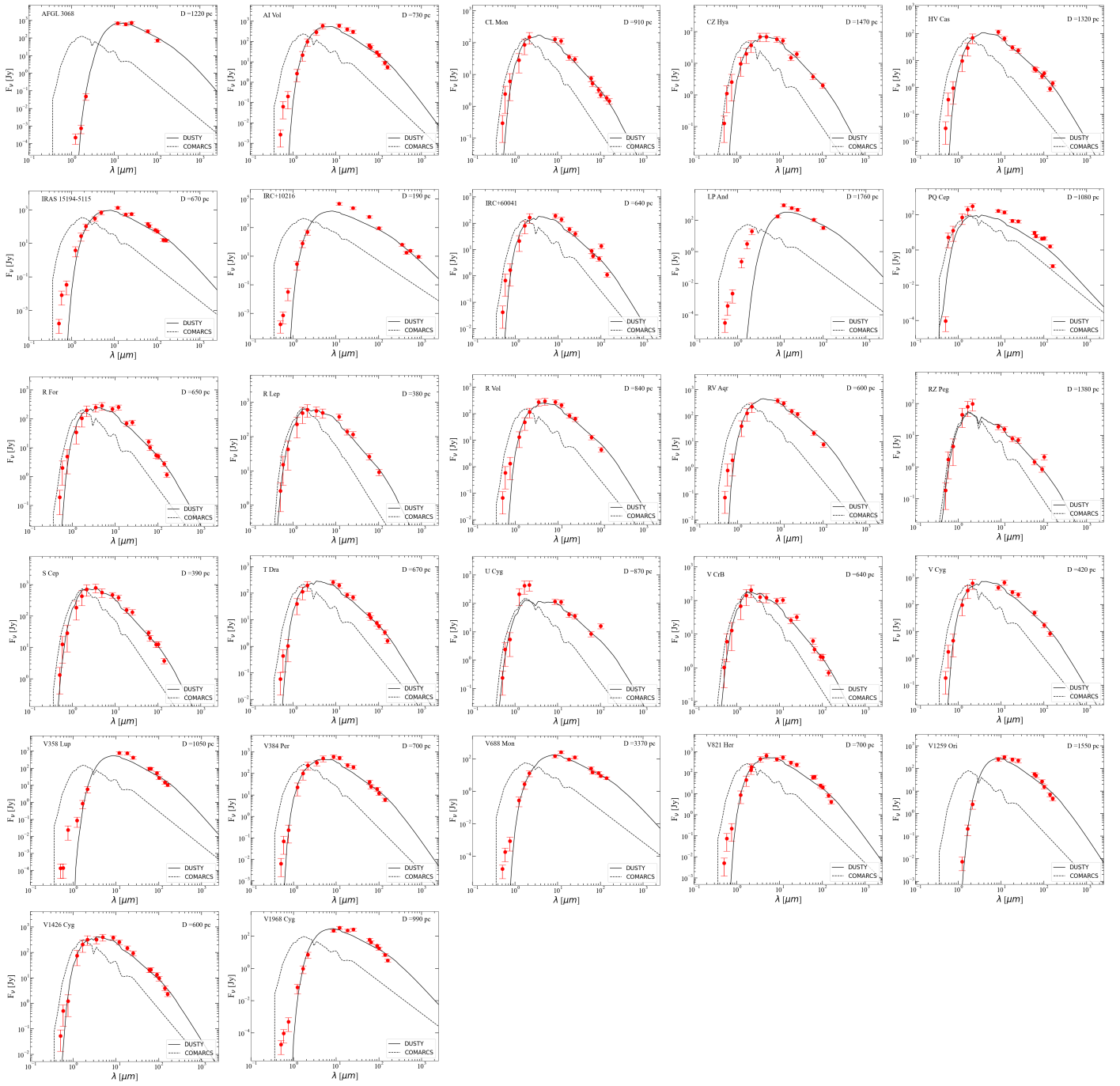


Fig. B.3. SED fitting of the stellar and dust emission of the C-type Miras in the DEATHSTAR sample with DUSTY. The name of each source is given in the upper left corner of each panel, and the derived distance is given in the upper right corner, in pc.

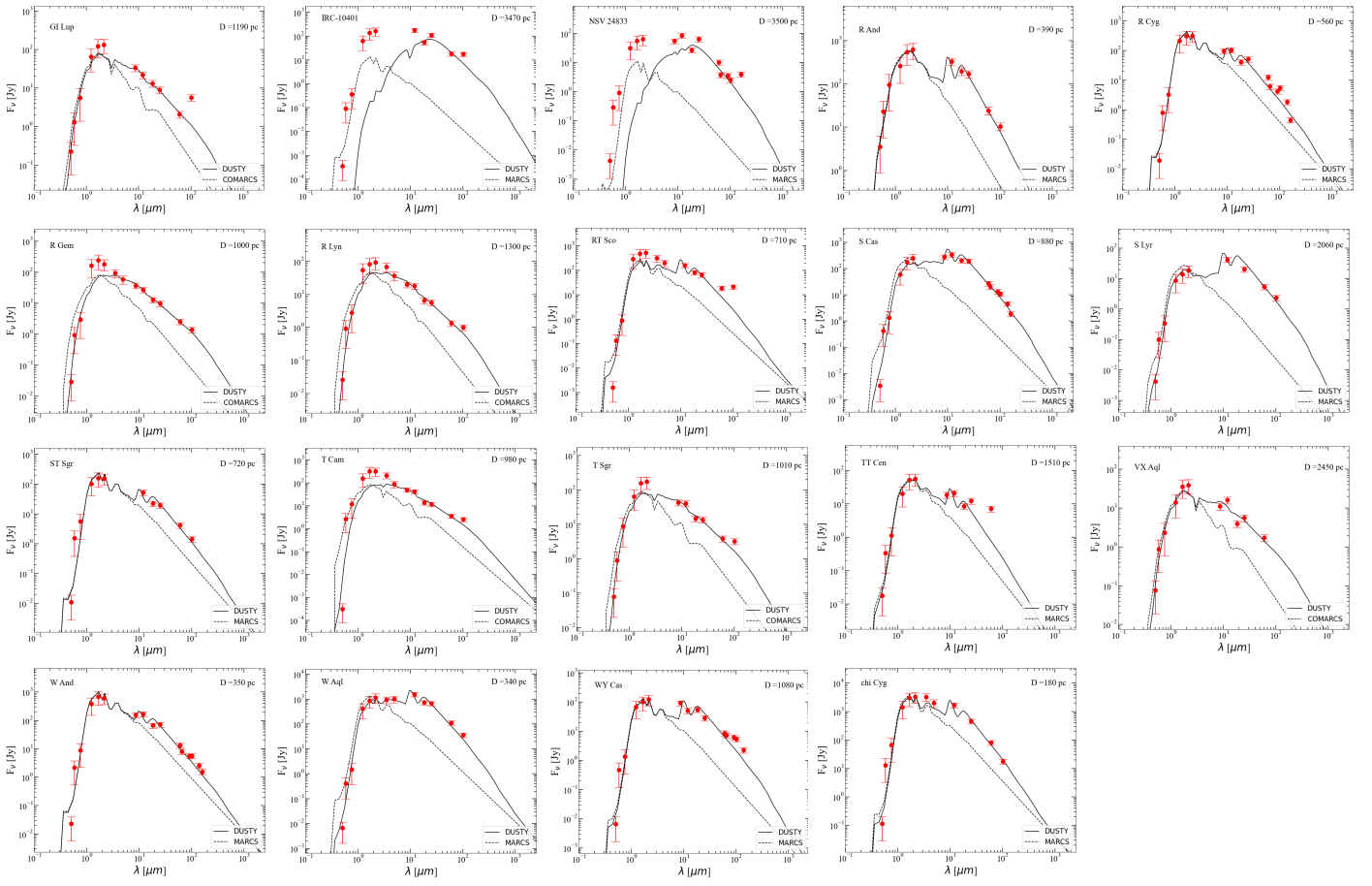


Fig. B.4. SED fitting of the stellar and dust emission of the S-type Miras in the DEATHSTAR sample with DUSTY. The name of each source is given in the upper left corner of each panel, and the derived distance is given in the upper right corner, in pc.

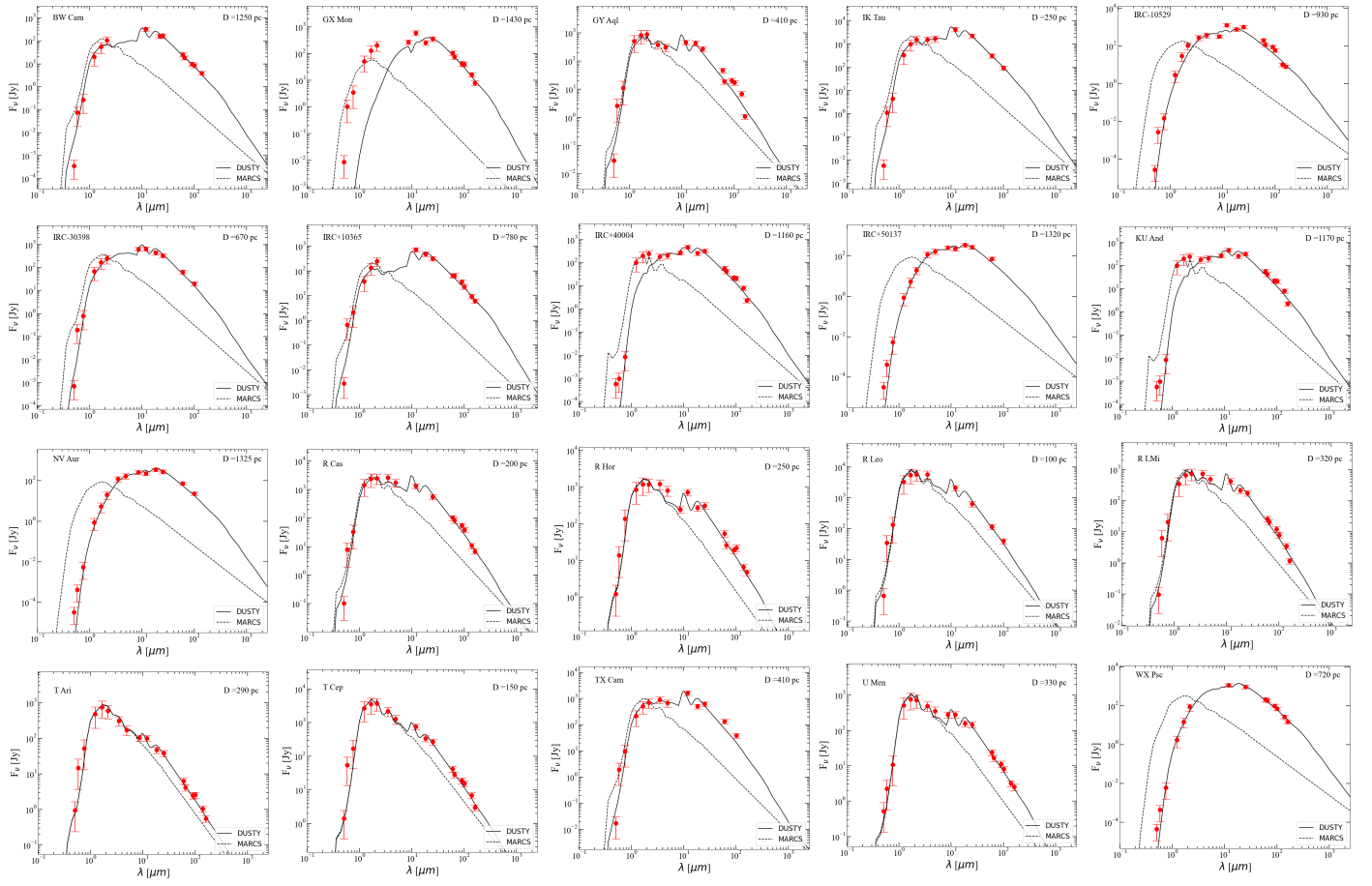


Fig. B.5. SED fitting of the stellar and dust emission for the M-type Miras in the DEATHSTAR sample with DUSTY. The name of each source is given in the upper left corner of each panel, and the derived distance is given in the upper right corner, in pc.

Appendix C: New distance catalogue

Table C.1. Best distance estimates for the DEATHSTAR sample. Table C.1. continued

Source	r_{median} [pc]	σ_r^- [pc]	σ_r^+ [pc]	Type	Spectral type	Source	r_{median} [pc]	σ_r^- [pc]	σ_r^+ [pc]	Type	Spectral type
AA Cam	489	60	79	G _{AGB}	S	IK Tau	289	54	88	G _{AGB}	M
AA Cyg	440	53	45	PL(SRb)	S	IRAS 15194-5115	696	93	129	G _{AGB}	C
AFGL 3068	1220	60	70	PL(M _{out})	C	IRC+10216	190	20	20	PL(M _{out})	C
AH Dra	391	34	44	PL(SRb)	M	IRC+10365	519	82	122	G _{AGB}	M
AI Vol	583	56	70	G _{AGB}	C	IRC+40004	1160	60	70	PL(M _{out})	M
AM Cen	897	103	134	G _{AGB}	S	IRC+60041	1300	175	241	G _{AGB}	C
AP Lyn	501	10	10	V	M*	IRC-10401	3470	120	110	PL(M)	S
AQ And	768	72	89	G _{AGB}	C	IRC-10529	930	70	60	PL(M _{out})	OH/IR
AQ Sgr	470	51	57	PL(SRb)	C	IRC-30398	670	50	40	PL(M _{out})	M
BD+06 319	312	52	80	G _{AGB}	M	KU And	1170	70	60	PL(M _{out})	M
BK Vir	242	39	59	G _{AGB}	M	L ² Pup	102	10	14	PL(SRb)	M
BL Ori	437	49	52	PL(SRb)	C	LP And	428	40	50	G _{AGB}	C
BM Gem	1243	201	293	G _{AGB}	C	NP Pup	586	70	91	G _{AGB}	C
BW Cam	1250	50	60	PL(M _{out})	OH/IR	NSV 17351	4064	157	168	V	OH/IR
BX Cam	579	10	10	V	M	NSV 24833	3500	120	140	PL(M)	S
BX Eri	476	23	25	V	M	NV Aur	1325	65	65	PL(M _{out})	M
CL Mon	910	30	40	PL(M)	C	OH 56.1 +2.1	3953	616	392	G _{AGB}	U
CS Dra	457	69	99	G _{AGB}	M	OZ Gem	1246	58	63	V	M*
CSS2 41	3792	700	497	G _{AGB}	S	PQ Cep	631	45	54	G _{AGB}	C
CW Cnc	262	27	35	G _{AGB}	M	QX Pup	1652	78	86	V	OH/IR
CZ Hya	1514	253	364	G _{AGB}	C	R And	390	30	20	PL(M)	S
DK Vul	843	80	88	PL(SRa)	S	R Aqr	220	11	12	V	M
DR Ser	1200	223	369	G _{AGB}	C	R Cas	200	10	2	PL(M)	M
DY Gem	644	76	62	PL(SRa)	S	R Cnc	266	19	22	V	M
EP Aqr	103	10	13	PL(SRb)	M	R CrA	237	40	64	G _{AGB}	M
EP Vul	461	45	56	PL(SRb)	S	R Cyg	555	45	54	G _{AGB}	S
FU Mon	795	99	132	G _{AGB}	S	R Dor	44	4	5	PL(SRb)	M
FV Boo	1034	60	67	V	M*	R For	507	24	27	G _{AGB}	C
GI Lup	1019	169	254	G _{AGB}	S	R Gem	847	159	256	G _{AGB}	S
GX Mon	1430	70	70	PL(M _{out})	OH/IR	R Hor	260	48	77	G _{AGB}	M
GY Aql	340	31	30	PL(M)	M	R Hya	126	2	3	V	M
HS UMa	356	11	13	V	M	R LMi	320	10	10	PL(M)	M
HU Pup	3437	426	511	V	M	R Leo	100	5	5	PL(M)	M
HV Cas	1205	163	225	G _{AGB}	C	R Lep	471	64	88	G _{AGB}	C
						R Lyn	880	105	138	G _{AGB}	S
						R Peg	374	36	44	V	M
						R Scl	408	61	86	G _{AGB}	C
						R UMa	508	12	14	V	M
						R Vol	662	68	86	G _{AGB}	C
						RR Aql	411	11	12	V	M
						RS And	327	34	36	PL(SRa)	M
						RS CrA	1467	97	112	G _{AGB}	U
						RT Cap	564	69	92	G _{AGB}	C
						RT Sco	710	60	60	PL(M)	S
						RT Vir	227	6	7	V	M
						RV Aqr	586	50	61	G _{AGB}	C
						RV Cam	382	41	36	PL(SRb)	M

r_{median} is the median distance.
 $\sigma_r^-/+$ the lower/upper distance uncertainty.
V: VLBI; G: Gaia.
PL(M): PL relation for Miras (this work).
PL(M_{out}): PL(M) outside the period range.
PL(SRa/b): PL relation for SRa/b by Knapp et al. (2003).
(:) indicates that the SR type is unknown.
Spectral types: M (C<O), S (C~O),
C (C>O), OH/IR (see text).
M*: suspected OH/IR, U: not defined in SIMBAD.

Table C.1. continued.

Source	r_{median} [pc]	σ_r^- [pc]	σ_r^+ [pc]	Type	Spectral type
RV Cyg	488	49	58	PL(SRb)	C
RW LMi	319	22	27	G _{AGB}	C
RW Lep	636	59	72	V	M
RX Boo	139	9	11	V	M
RX Lac	378	51	38	PL(SRb)	S
RY Dra	401	38	47	G _{AGB}	C
RY Mon	875	96	124	G _{AGB}	C
RZ Peg	1275	128	161	G _{AGB}	C
RZ Sgr	432	50	66	G _{AGB}	S
S Aur	1057	112	133	PL(SR:)	C
S Cas	880	60	50	PL(M _{out})	S
S Cep	534	93	144	G _{AGB}	C
S CrB	424	28	33	V	M
S Crb	433	23	25	V	M
S Dra	253	27	24	PL(SRb)	M
S Lyr	2060	80	80	PL(M)	S
S Pav	184	16	17	PL(SRa)	M
S Sct	438	50	65	G _{AGB}	C
S Ser	801	25	27	V	M
SS Vir	583	112	173	G _{AGB}	C
ST Cam	625	91	129	G _{AGB}	C
ST Her	324	57	86	G _{AGB}	S
ST Sco	412	48	38	PL(SRa)	S
ST Sgr	720	40	70	PL(M)	S
SU Vel	417	68	103	G _{AGB}	M
SV Aqr	445	65	90	G _{AGB}	M
SV Peg	334	7	7	V	M
SW Vir	125	16	12	PL(SRb)	M
SY Aql	922	56	64	V	OH/IR
SY Scl	1330	50	55	V	M
SZ Car	689	45	52	G _{AGB}	C
SZ Dra	470	57	75	G _{AGB}	M
T Ari	290	5	10	PL(M)	M
T Cam	980	30	40	PL(M)	S
T Cep	150	2	2	PL(M)	M
T Cet	213	24	23	PL(SRb)	M
T Dra	901	146	214	G _{AGB}	C
T Ind	467	38	66	PL(SRb)	C
T Lep	327	4	4	V	M
T Lyr	427	33	38	G _{AGB}	C
T Mic	175	15	19	PL(SRb)	M
T Sgr	1010	50	50	PL(M)	S
TT Cen	1182	152	208	G _{AGB}	S
TT Cyg	671	43	49	G _{AGB}	C
TT Tau	671	59	73	G _{AGB}	C
TU Gem	497	51	57	PL(SRb)	C
TV Dra	541	90	134	G _{AGB}	M

Table C.1. continued.

Source	r_{median} [pc]	σ_r^- [pc]	σ_r^+ [pc]	Type	Spectral type
TW Hor	481	75	109	G _{AGB}	C
TW Oph	392	38	46	PL(SRb)	C
TW Peg	278	48	77	G _{AGB}	M
TX Cam	292	35	47	G _{AGB}	M
TY Dra	699	89	120	G _{AGB}	M
TZ Aql	524	64	84	G _{AGB}	M
U Ant	294	40	54	G _{AGB}	C
U Cam	630	77	102	G _{AGB}	C
U Cyg	687	37	41	G _{AGB}	C
U Her	271	19	21	V	M
U Hya	286	34	31	PL(SRb)	C
U Lyn	792	36	39	V	M
U Men	317	28	34	G _{AGB}	M
UU Aur	306	30	40	PL(SRb)	C
UX And	321	28	41	PL(SRb)	M
UX Cyg	1918	198	250	V	M
UX Dra	373	37	39	PL(SRb)	C
UY Cen	718	127	200	G _{AGB}	S
UY Cet	449	50	51	PL(SRb)	M
V Aql	379	39	38	PL(SRb)	C
V CrB	836	81	99	G _{AGB}	C
V Cyg	420	10	20	PL(M)	C
V Hya	311	35	36	PL(SRa)	C
V tel	423	47	42	PL(SRb)	M
V1259 Ori	1550	90	90	PL(M _{out})	C
V1302 Cen	892	91	114	G _{AGB}	C
V1426 Cyg	709	113	168	G _{AGB}	C
V1942 Sgr	650	84	115	G _{AGB}	C
V1943 Sgr	189	22	19	PL(SRb)	M
V1968 Cyg	990	80	100	PL(M)	C
V358 Lup	1050	60	60	PL(M _{out})	C
V365 Cas	464	48	49	PL(SRb)	S
V384 Per	700	30	30	PL(M _{out})	C
V386 Cep	1037	85	137	PL(SRb)	M
V460 Cyg	360	37	44	PL(SRb)	C
V466 Per	685	84	112	G _{AGB}	C
V637 Per	1065	22	23	V	M
V688 Mon	3370	250	260	PL(M _{out})	C
V821 Her	700	61	50	PL(M _{out})	C
V837 Her	918	9	8	V	M
V996 Cen	578	59	74	G _{AGB}	C
VX And	619	49	59	G _{AGB}	C
VX Aql	2450	110	120	PL(M _{out})	S
VY UMa	444	71	104	G _{AGB}	C
W And	350	20	20	PL(M)	S
W Aql	380	49	68	G _{AGB}	S
W CMa	777	148	246	G _{AGB}	C

Table C.1. continued.

Source	r_{median} [pc]	σ_r^- [pc]	σ_r^+ [pc]	Type	Spectral type
W Hya	87	9	11	PL(SRa)	M
W Leo	971	18	19	V	M
W Ori	260	24	28	PL(SRb)	C
W Pic	594	43	49	G _{AGB}	C
WX Psc	720	30	30	PL(M _{out})	OH/IR
WY Cas	1141	196	302	G _{AGB}	S
WZ Cas	465	33	38	G _{AGB}	C
X Cnc	332	36	41	PL(SRb)	C
X Her	137	23	34	G _{AGB}	M
X Hya	484	11	12	V	M
X TrA	292	39	28	PL(SR:)	C
X Vel	631	65	82	G _{AGB}	C
XZ Vel	1151	162	228	G _{AGB}	C
Y CVn	249	22	25	PL(SRb)	C
Y Hya	451	36	65	PL(SRb)	C
Y Lib	1173	64	73	V	M
Y Lyn	200	21	24	PL(SR:)	S
Y Pav	381	37	56	PL(SRb)	C
Y Scl	504	50	54	PL(SRb)	M
Y Tau	409	43	40	PL(SRb)	C
Y Tel	442	77	118	G _{AGB}	M
Y UMa	348	57	83	G _{AGB}	M
ZZ Ant	580	54	68	PL(SR:)	S
Z Psc	660	107	157	G _{AGB}	C
θ Aps	104	11	13	PL(SRb)	M
χ Cyg	180	10	5	PL(M)	S